Competition between Raman- and Rayleigh-enhanced four-wave mixings in attosecond polarization beats

Chenli Gan,[1,2] Yanpeng Zhang,[1,2,*] Zhiqiang Nie,[1] Yan Zhao,[1] Keqing Lu,[3] Jinhai Si,[1] and Min Xiao[2]
[1]*Key Laboratory for Physical Electronics and Devices of the Ministry of Education, Xi'an Jiaotong University, Xi'an 710049, China*
[2]*Department of Physics, University of Arkansas, Fayetteville, Arkansas 72701, USA*
[3]*State Key Laboratory of Transient Optics and Technology, Xi'an Institute of Optics and Precision Mechanics, Chinese Academy of Sciences, Xi'an 710068, China*
(Received 23 May 2008; published 2 February 2009)

Based on color-locking noisy field correlation, the subtle Markovian field correlation effects in three stochastic models have been investigated in studying the Raman- and Rayleigh-enhanced four-wave mixing (FWM). Homodyne and heterodyne detections of the Raman attosecond sum-frequency polarization beats (ASPB), the Rayleigh ASPB, and the coexisting Raman and Rayleigh ASPB have also been investigated, respectively. Raman- and Rayleigh-enhanced FWM processes strongly compete with each other in ASPB. The heterodyne detected signal of ASPB potentially offers rich dynamic information about the homogeneous broadening material phase of the third-order nonlinear susceptibility.

DOI: 10.1103/PhysRevA.79.023802 PACS number(s): 42.65.Es, 42.65.Re, 42.50.Ar, 42.65.Hw

I. INTRODUCTION

Lasers are inherently noisy devices, in which both the phase and amplitude of the field can fluctuate. Noisy light can be used to probe atomic and molecular dynamics, and it offers a unique alternative to the more conventional frequency domain spectroscopies and ultrashort pulse time domain spectroscopies. Color locking noisy light is an intermediate between cw and short-pulse methods [1–9]. Color locking can result in complete cancellation of the spectrally broad noise carried by the noisy light [2].

Phase locking ultrashort-pulse nonlinear optical spectroscopy has proved to be a valuable technique for investigating the dynamics of a wealth of mechanisms in condensed matters. Four-wave mixing (FWM) is a third-order nonlinear optical process [10,11]. Using femtosecond time-resolved FWM, valuable information on the dephasing dynamics in semiconductors and molecular materials has been obtained. The time resolution of this method is limited by the pulse width. However, the ultrafast dephasing phenomena can also be studied by time-delayed FWM with incoherent light [1]. This technique is intrinsically related to the optical coherent transient spectroscopy with an advantage that the time resolution is determined by the correlation time τ_c of the color locking noisy light source. Since the relaxation time is deduced from the FWM spectrum, the measurement is not limited by the laser pulse width [1].

The atomic response to Markovian stochastic optical fields is now largely well understood [12–15]. When the laser field is sufficiently intense that many photon interactions occur, the laser spectral bandwidth or spectral shape, obtained from the second-order correlation function, is inadequate to characterize the field. Rather than using higher-order correlation functions explicitly, three different Markovian fields are considered: (a) the chaotic field, (b) the phase-diffusion field, and (c) the Gaussian-amplitude field. The chaotic field undergoes both amplitude and phase fluctuations and corresponds to a multimode laser field with a large number of uncorrelated modes, or a single-mode laser emitting light below threshold. Since a chaotic field does not possess any intensity stabilization mechanism, the field can take on any value in a two-dimensional region of the complex plane centered about the origin [15]. The phase-diffusion field undergoes only phase fluctuations and corresponds to an intensity-stabilized single-mode laser field. The phase of the laser field, however, has no natural stabilizing mechanism [15]. The Gaussian-amplitude field undergoes only amplitude fluctuations. There is no such obvious natural source for a real Gaussian field. However, one can generate it through intentionally modulating the cw laser with the acousto-optic modulator [13,16]. We do consider the Gaussian-amplitude field for two reasons. First, because it allows us to isolate those effects due solely to amplitude fluctuations and second, because it is an example of a field that undergoes stronger amplitude (intensity) fluctuations than a chaotic field. By comparing the results for the chaotic and the Gaussian-amplitude fields we can determine the effect of increasing amplitude fluctuations [17,18].

Laser-induced gratings have received considerable attention because of their potential applications in spectroscopy and phase conjugation. When two pump beams with the same frequency interfere in liquids, the optical Kerr effect [19] results in the generation of a molecular-reorientation grating. Moreover, if the absorption coefficient of a sample at the pump beam frequency is not zero, the molecular-reorientation grating is usually accompanied by an undesired thermal grating [20]. In this case, FWM signal can be the Bragg reflection of the probe beam by the molecular-reorientation grating and the thermal grating induced by the two pump beams [21–26].

Coherent Raman spectroscopy (CRS) is a powerful tool for studying the vibrational or rotational mode of a molecule. In Raman-enhanced FWM (one of the CRS techniques) [21,23–26], the Raman vibration is excited by the simultaneous presence of two incident beams whose frequency dif-

*ypzhang@mail.xjtu.edu.cn

ference equals the Raman excitation frequency and the Raman-enhanced FWM signal is the result of this resonant excitation. In contrast, Rayleigh-enhanced FWM [22,26] is a nonresonant process with no energy transfer between the lights and the medium when the frequency difference between two incident beams equals zero. The resonant structure in Rayleigh-enhanced FWM spectrum is the result of induced moving grating. The Raman- or Rayleigh-enhanced FWM may be superior to all other CRS techniques [23–26]. They possess the features of nonresonant background suppression, excellent spatial signal resolution, free choice of interaction volume, and simple optical alignment. Moreover, phase matching can be achieved for a very wide frequency range from many hundreds to thousands of cm^{-1}.

Polarization beat between two excitation pathways is related to recent studies on quantum interference [27–29]. DeBeer *et al.* [27] performed the 980-as-sum-frequency ultrafast modulation spectroscopy (UMS) experiment. Bogdanov *et al.* have also showed the attosecond beats with different sources: an interference of the Rayleigh scattering field and the FWM field of phase-locking ultrashort laser pulses [28]. The Raman- and Rayleigh-enhanced attosecond sum-frequency polarization beats (ASPB) are the interesting ways to study the stochastic properties of light [23–26]. The characteristics of the interferogram of Raman- and Rayleigh-enhanced ASPB are a result of two main components: the material response and the light response along with the interplay between the two responses.

This paper addresses the role of noise in the incident fields on the nature of the wave-mixing signal in the time and frequency domains. This important topic has been already treated extensively in the literature [13]. Ulness *et al.* invented the factorized time correlator diagram "synchronization" and "accumulation" analysis for noisy light response [2–9], instead of double-sided Feynman diagrams. A fundamental principle of noisy light spectroscopy is color locking, which results as a consequence of the phase-incoherent nature of the light. Color locking can be responsible for the complete and utter cancellation of the noise spectrum carried by the noisy light used to produce it [2]. On the other hand, there should be two classes of such two component beams. In one class the components are derived from separate lasers and their mixed (cross) correlators should vanish. In the second case the two components are derived from a single laser source whose spectral output is doubly peaked. This can be created from a single dye laser in which two different dyes in solution together are amplified [6–9]. The present paper deals only with the first class, where the doubled peaked beams 1 and 2 are paired and correlated, but each of the peaks is uncorrelated, while beam 3 is from another noisy light source with a single peak, and independent and uncorrelated to twin beams 1 and 2, which are shown in Fig. 1.

In this paper, based on the field correlation of color-locking twin noisy lights, the Raman- and Rayleigh-enhanced FWM, and the homodyne, heterodyne detection of pure Raman, pure Rayleigh, and coexistence of Raman and Rayleigh ASPB have been investigated, respectively. Raman- and Rayleigh-enhanced FWM compete with each other in the coexistence of Raman and Rayleigh ASPB. An analytic closed form of results is obtained.

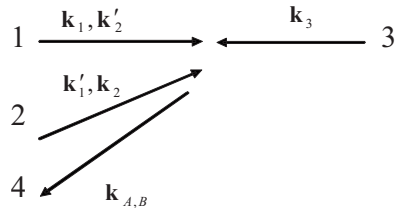

FIG. 1. Phase-conjugation geometry of the ASPB.

The paper is organized as follows. Section II presents the basic theory of field-correlation effects on the Raman- and Rayleigh-enhanced FWM. We give the three schemes of the pure Raman ASPB, the pure Rayleigh ASPB and the coexisting Raman and Rayleigh ASPB. Section III presents the Rayleigh- and Raman-enhanced FWM in three Markovian stochastic models. In addition, a time-delayed method to suppress the background is mentioned in a Kerr medium and an absorbing medium. Section IV gives the Raman- and Rayleigh-enhanced nonlinear susceptibility with cw laser beams. In Secs. V and VI the homodyne and heterodyne detection of three types of ASPB are shown. Section VII gives the discussion and conclusion.

II. BASIC THEORY

The Raman and Rayleigh ASPB are the third-order nonlinear polarization beat phenomenon. Here polarization beat is based on the interference at the detector between two FWM signals which originate from macroscopic polarizations excited simultaneously in the homogeneous or inhomogeneous broadening sample. It requires that all the polarizations have the same frequency.

The basic geometry is shown in Fig. 1. Twin beams 1 and 2 consist of two frequency components ω_1 and ω_2, a small angle exists between them. Beam 3 with frequency ω_3 is almost propagating along the opposite direction of beam 1. Twin composite stochastic fields of beam 1, $E_{p1}(\mathbf{r},t)$, and beam 2, $E_{p2}(\mathbf{r},t)$ for homodyne detection scheme, can be written as

$$\begin{aligned} E_{p1} &= E_1(\mathbf{r},t) + E'_2(\mathbf{r},t) \\ &= A_1(\mathbf{r},t)\exp(-i\omega_1 t) + A'_2(\mathbf{r},t)\exp[-i\omega_2(t-\tau)] \\ &= \varepsilon_1 u_1(t)\exp[i(\mathbf{k}_1\cdot\mathbf{r}-\omega_1 t)] \\ &\quad + \varepsilon'_2 u_2(t-\tau)\exp[i(\mathbf{k}'_2\cdot\mathbf{r}-\omega_2 t+\omega_2\tau)], \\ E_{p2} &= E'_1(\mathbf{r},t) + E_2(\mathbf{r},t) \\ &= A'_1(\mathbf{r},t)\exp[-i\omega_1(t-\tau)] + A_2(\mathbf{r},t)\exp(-i\omega_2 t) \\ &= \varepsilon'_1 u_1(t-\tau)\exp[i(\mathbf{k}'_1\cdot\mathbf{r}-\omega_1 t+\omega_1\tau)] \\ &\quad + \varepsilon_2 u_2(t)\exp[i(\mathbf{k}_2\cdot\mathbf{r}-\omega_2 t)]. \end{aligned} \tag{1}$$

Here, $\varepsilon_i, \mathbf{k}_i$ $(\varepsilon'_i, \mathbf{k}'_i)$ are the constant field amplitude and the wave vector of the ω_i component in beams 1 and 2, respectively. $u_i(t)$ is a dimensionless statistical factor that contains phase and amplitude fluctuations. It is taken to be a complex ergodic stochastic function of t, which obey complex circular Gaussian statistics in chaotic field. τ is a variable relative

time delay between the prompt (unprime) and delayed (prime) fields. To accomplish this the frequency component ω_1 and ω_2 lights are split and recombined to provide two double-frequency pulses in such a way that the ω_1 component is delayed by τ in beam 2 and the ω_2 component delayed by the same amount in the beam 1 (Fig. 1). The time delay τ is introduced in both composite beams, which is quite different with that of femtosecond difference-frequency polarization beats [23–26]. On the other hand, the complex electric fields of beam 3 can be written as $E_3(\mathbf{r},t) = A_3(\mathbf{r},t)\exp(-i\omega_3 t) = \varepsilon_3 u_3(t)\exp[i(\mathbf{k}_3\cdot\mathbf{r}-\omega_3 t)]$. Here, ω_3, ε_3, and $\mathbf{k}_3$ are the frequency, the field amplitude, and the wave vector of the field, respectively.

In an absorbing medium, the nonlinear interaction of beams 1 and 2 with the medium gives rise to the molecular-reorientation gratings and the thermal gratings, i.e., $\omega_{1,2}$ will induce their own nonresonant static molecular-reorientation gratings $G_{M1,2}$ and thermal gratings $G_{T1,2}$. The FWM signals are the results of the diffraction of beam 3 by these four gratings, respectively. The order parameters Q_{M1}, Q_{T1}, Q_{M2}, and Q_{T2} of four nonresonant static gratings satisfy the following equations [19,20]:

$$dQ_{M1}/dt + \gamma_M Q_{M1} = \chi_M \gamma_M E_1(\mathbf{r},t)[E_1'(\mathbf{r},t)]^*,$$

$$dQ_{T1}/dt + \gamma_T Q_{T1} = \chi_T \gamma_T E_1(\mathbf{r},t)[E_1'(\mathbf{r},t)]^*,$$

$$dQ_{M2}/dt + \gamma_M Q_{M2} = \chi_M \gamma_M E_2'(\mathbf{r},t)[E_2(\mathbf{r},t)]^*,$$

$$dQ_{T2}/dt + \gamma_T Q_{T2} = \chi_T \gamma_T E_2'(\mathbf{r},t)[E_2(\mathbf{r},t)]^*. \quad (2)$$

Here $\gamma_{M,T}$ and $\chi_{M,T}$ are the relaxation rate and the nonlinear susceptibility of the molecular-reorientation grating and thermal grating, respectively.

Now if the frequency difference $\Delta_1 = \omega_3 - \omega_1$ is much smaller than $\Delta'_1 = \omega_3 - \omega_2$ (i.e., $\Delta_1 \ll \Delta'_1$ and $\Delta_1 \approx 0$) and the frequency detuning $\Delta_2 = \Delta'_1 - \Omega_R$ is near zero, the coexisting Raman and Rayleigh modes of the medium enhance the FWM signals. Here Ω_R is the Raman resonant frequency. Specifically, on one hand, two resonant moving gratings, G_{RM} and G_{RT} with large angle formed by the interference between the ω_1 frequency component of beam 2 and the ω_3 frequency component of beam 3, will excite the Rayleigh mode of the medium and enhance the FWM signals corresponding to G_{M1} and G_{T1} (i.e., Rayleigh-enhanced FWM). On the other hand, one large resonant moving grating, G_R formed by the interference between the ω_2 frequency component of beam 2 and the ω_3 frequency component of beam 3, will excite the Raman mode of the medium and enhance the FWM signals corresponding to G_{M2} and G_{T2} (i.e., Raman-enhanced FWM). The order parameters Q_R, Q_{RT}, and Q_{RM} satisfy the following equations [19,21–26]:

$$dQ_R/dt + (\gamma_R - i\Delta_2)Q_R = \chi_R \gamma_R [E_2(\mathbf{r},t)]^* E_3(\mathbf{r},t),$$

$$dQ_{RM}/dt + \gamma_M Q_{RM} = \chi_M \gamma_M [E_1'(\mathbf{r},t)]^* E_3(\mathbf{r},t),$$

$$dQ_{RT}/dt + \gamma_T Q_{RT} = \chi_T \gamma_T [E_1'(\mathbf{r},t)]^* E_3(\mathbf{r},t). \quad (3)$$

Based on Eqs. (2) and (3) shown above, the induced seven third-order nonlinear polarizations which are responsible for the FWM signals are

$$P_{M1} = Q_{M1}(\mathbf{r},t)E_3(\mathbf{r},t) = \chi_M \gamma_M S_1(\mathbf{r})\varepsilon_1(\varepsilon_1')^*\varepsilon_3 \times \int_0^\infty u_1(t-t')u_1^*(t-t'-\tau)u_3(t)\exp(-\gamma_M t')dt', \quad (4)$$

$$P_{T1} = Q_{T1}(\mathbf{r},t)E_3(\mathbf{r},t) = \chi_T \gamma_T S_1(\mathbf{r})\varepsilon_1(\varepsilon_1')^*\varepsilon_3 \times \int_0^\infty u_1(t-t')u_1^*(t-t'-\tau)u_3(t)\exp(-\gamma_T t')dt', \quad (5)$$

$$P_{M2} = Q_{M2}(\mathbf{r},t)E_3(\mathbf{r},t) = \chi_M \gamma_M S_2(\mathbf{r})(\varepsilon_2)^*\varepsilon_2'\varepsilon_3 \times \int_0^\infty u_2^*(t-t')u_2(t-t'-\tau)u_3(t)\exp(-\gamma_M t')dt', \quad (6)$$

$$P_{T2} = Q_{T2}(\mathbf{r},t)E_3(\mathbf{r},t) = \chi_T \gamma_T S_2(\mathbf{r})(\varepsilon_2)^*\varepsilon_2'\varepsilon_3 \times \int_0^\infty u_2^*(t-t')u_2(t-t'-\tau)u_3(t)\exp(-\gamma_T t')dt', \quad (7)$$

$$P_R = Q_R(\mathbf{r},t)E_2'(\mathbf{r},t) = i\chi_R \gamma_R S_2(\mathbf{r})(\varepsilon_2)^*\varepsilon_3\varepsilon_2' \times \int_0^\infty u_2^*(t-t')u_3(t-t')u_2(t-\tau)\exp[-(\gamma_R - i\Delta_2)t']dt', \quad (8)$$

$$P_{RM} = Q_{M1}(\mathbf{r},t)E_1(\mathbf{r},t) = \chi_M \gamma_M S_1(\mathbf{r})(\varepsilon_1')^*\varepsilon_3\varepsilon_1 \times \int_0^\infty u_1^*(t-t'-\tau)u_3(t-t')u_1(t) \times \exp[-(\gamma_M - i\Delta_1)t']dt', \quad (9)$$

$$P_{RT} = Q_{T1}(\mathbf{r},t)E_1(\mathbf{r},t) = \chi_T \gamma_T S_1(\mathbf{r})(\varepsilon_1')^*\varepsilon_3\varepsilon_1 \times \int_0^\infty u_1^*(t-t'-\tau)u_3(t-t')u_1(t)\exp[-(\gamma_T - i\Delta_1)t']dt'. \quad (10)$$

Here $S_1(\mathbf{r})=\exp\{i[(\mathbf{k}_1-\mathbf{k}'_1+\mathbf{k}_3)\cdot\mathbf{r}-\omega_3 t-\omega_1\tau]\}$ and $S_2(\mathbf{r})=\exp\{i[(\mathbf{k}'_2-\mathbf{k}_2+\mathbf{k}_3)\cdot\mathbf{r}-\omega_3 t+\omega_2\tau]\}$. Therefore, polarization $P_A=P_{M2}+P_{T2}+P_R$ corresponding to the Raman-enhanced FWM process with phase-matching condition $\mathbf{k}'_2-\mathbf{k}_2+\mathbf{k}_3$ and $P_B=P_{M1}+P_{T1}+P_{RM}+P_{RT}$ corresponding to the Rayleigh-enhanced FWM process with phase-matching condition $\mathbf{k}_1-\mathbf{k}'_1+\mathbf{k}_3$. Both FWM signals have the same frequency, i.e., ω_3. As a result, ASPB originates from the interference between the macroscopic polarizations from the Rayleigh-enhanced FWM and the Raman-enhanced FWM signals. The beat signal (beam 4) is along the opposite direction of beam 2 approximately [23–29].

Furthermore, if the ω_1, ω_2, and ω_3 frequency components of the beams only satisfy the excitation condition of Rayleigh mode where $\Delta_1 \ll \Delta'_1$ and $\Delta_1 \approx 0$, the Raman-enhanced FWM polarization P_A converts into the FWM polarization $P_C=P_{M2}+P_{T2}$ and we have the pure Rayleigh ASPB based on the interference at the detector between FWM signals resulted from P_B and P_C. Similarly, we can have the pure Raman ASPB resulted from P_A and $P_D=P_{M1}+P_{T1}$ if only the excitation condition of Raman mode is satisfied and the Rayleigh-enhanced FWM polarization P_B converts into the FWM polarization P_D.

To be brief, with the geometry shown in Fig. 1, under the excitation condition of Raman mode the beams $\mathbf{k}_2$ and $\mathbf{k}'_2$ generate Raman-enhanced FWM (P_A); under the excitation condition of Rayleigh mode the beams $\mathbf{k}_1$ and $\mathbf{k}'_1$ generate Rayleigh-enhanced FWM (P_B). When only one condition is satisfied, we obtain pure Raman ASPB ($P_A+P_D=P_{M2}+P_{T2}+P_R+P_{M1}+P_{T1}$) or Rayleigh ASPB ($P_B+P_C=P_{M1}+P_{T1}+P_{RM}+P_{RT}+P_{M2}+P_{T2}$). However, when both the excitation conditions are fulfilled, Raman- and Rayleigh-enhanced FWM interact with each other to generate the coexisting Raman and Rayleigh ASPB ($P_A+P_B=P_{M2}+P_{T2}+P_R+P_{M1}+P_{T1}+P_{RM}+P_{RT}$).

III. STOCHASTIC CORRELATION EFFECTS OF RAYLEIGH- AND RAMAN-ENHANCED FWM

We have the total third-order polarization P_A (P_B) for Raman- (Rayleigh-) enhanced FWM. For the macroscopic system where phase matching takes place the signal must be drawn from the P_A (P_B) developed on one "atom" multiplied by the P_A^* (P_B^*) that is developed on another "atom" which must be located elsewhere in space (with summation over all such pairs). For homodyne detection the Raman—(Rayleigh-) enhanced FWM signal is proportional to the average of the absolute square of P_A (P_B) over the random variable of the stochastic process. We can have

$$\begin{aligned}\langle|P_A|^2\rangle &= \langle P_{M2}P^*_{M2}\rangle + \langle P_{M2}P^*_{T2}\rangle + \langle P_{M2}P^*_{R}\rangle + \langle P_{T2}P^*_{M2}\rangle \\ &+ \langle P_{T2}P^*_{T2}\rangle + \langle P_{T2}P^*_{R}\rangle + \langle P_{R}P^*_{M2}\rangle + \langle P_{R}P^*_{T2}\rangle \\ &+ \langle P_{R}P^*_{R}\rangle\end{aligned}$$

and

$$\begin{aligned}\langle|P_B|^2\rangle &= \langle P_{M1}P^*_{M1}\rangle + \langle P_{M1}P^*_{T1}\rangle + \langle P_{M1}P^*_{RM}\rangle + \langle P_{M1}P^*_{RT}\rangle \\ &+ \langle P_{T1}P^*_{M1}\rangle + \langle P_{T1}P^*_{T1}\rangle + \langle P_{T1}P^*_{RM}\rangle + \langle P_{T1}P^*_{RT}\rangle \\ &+ \langle P_{RM}P^*_{M1}\rangle + \langle P_{RM}P^*_{T1}\rangle + \langle P_{RM}P^*_{RM}\rangle + \langle P_{RM}P^*_{RT}\rangle \\ &+ \langle P_{RT}P^*_{M1}\rangle + \langle P_{RT}P^*_{T1}\rangle + \langle P_{RT}P^*_{RM}\rangle + \langle P_{RT}P^*_{RT}\rangle.\end{aligned}$$

They involves fourth- and second-order coherence functions of $u_i(t)$. For example, one terms of $\langle|P_A|^2\rangle$ is

$$\begin{aligned}\langle P_R P^*_{M2}\rangle &= i\chi_R\gamma_R\chi_M\gamma_M(\varepsilon_2)^*\varepsilon_3\varepsilon'_2 S_2(\mathbf{r})\varepsilon_2(\varepsilon'_2)^*(\varepsilon_3)^* S_2^*(\mathbf{r}) \\ &\times\int_0^\infty dt'\int_0^\infty ds'\langle u_2(t-\tau)u_2(t-s')u_2^*(t-t') \\ &\times u_2^*(t-s'-\tau)\rangle\langle u_3(t-t')u_3^*(t)\rangle \\ &\times\exp[-(\gamma_R-i\Delta_2)t'-\gamma_M s'].\end{aligned}$$

The fourth- and second-order coherence functions of $u_i(t)$ included in this equation are $\langle u_2(t-\tau)u_2(t-s')u_2^*(t-t')\times u_2^*(t-s'-\tau)\rangle$ and $\langle u_3(t-t')u_3^*(t)\rangle$, respectively.

If the laser sources have Lorentzian line shape, we have the second-order coherence function $\langle u_i(t_1)u_i^*(t_2)\rangle=\exp(-\alpha_i|t_1-t_2|)$ [i.e., $\langle|u_i(t)|^2\rangle=1$ when $t=t_1=t_2$]. Here $\alpha_i=\delta\omega_i/2$, $\delta\omega_i$ is the linewidth of the laser with frequency ω_i. On the other hand, if assuming that the laser sources have Gaussian line shape, then we have $\langle u_i(t_1)u_i^*(t_2)\rangle=\exp\{-[\alpha_i(t_1-t_2)/2\sqrt{\ln 2}]^2\}$. Here, we only consider the former. In fact, the form of the second-order coherence function shown above, which is determined by the laser line shape, is the general feature of the stochastic models [17,18].

In this paper, three Markovian noise stochastic models, the chaotic field model (CFM), the phase-diffusion model (PDM), and the Gaussian-amplitude model (GAM) are considered at the intensity level to fully appreciate the subtle features of FWM spectroscopy [30–33].

First of all, in CFM, we assume that the pump laser is a multimode thermal source and $u(t)=a(t)e^{i\phi(t)}$, where $a(t)$ is the fluctuating modulus and $\phi(t)$ is the fluctuating phase. In this case, $u(t)$ has Gaussian statistics with its fourth-order coherence function satisfying [22,23,34]

$$\begin{aligned}&\langle u_i(t_1)u_i(t_2)u_i*(t_3)u_i*(t_4)\rangle_{CFM} \\ &= \langle u_i(t_1)u_i*(t_3)\rangle\langle u_i(t_2)u_i*(t_4)\rangle \\ &+ \langle u_i(t_1)u_i*(t_4)\rangle\langle u_i(t_2)u_i*(t_3)\rangle \\ &= \exp[-\alpha_i(|t_1-t_3|+|t_2-t_4|)] \\ &+ \exp[-\alpha_i(|t_1-t_4|+|t_2-t_3|)].\end{aligned}$$

In fact, all higher-order coherence functions can be expressed in terms of products of second-order coherence functions. Thus any given $2n$ order coherence function may be decomposed into the sum of $n!$ terms, each consisting of the products of n second-order coherence function. The general expression can be obtained, $\langle u_i(t_1)\cdots u_i(t_n)u_i*(t_{n+1})\cdots\times u_i*(t_{2n})\rangle_{CFM}=\Sigma_\pi\langle u_i(t_1)u_i*(t_p)\rangle\langle u_i(t_2)u_i*(t_q)\rangle\cdots\langle u_i(t_n)u_i*\times(t_r)\rangle$, where Σ_π denotes a summation over the $n!$ possible permutations $(p,q,\ldots,r)$ of $(1,2,\ldots,n)$.

Secondly, in the PDM the dimensionless statistical factor can be written as $u(t)=e^{i\phi(t)}$ (i.e., $|u(t)|=1$) with $\dot{\phi}(t)=\omega(t)$, $\langle\omega_i(t)\omega_i(t')\rangle=2\alpha_i\delta(t-t')$, $\langle\omega_j(t)\omega_j(t')\rangle=2\alpha_j\delta(t-t')$, and $\langle\omega_i(t)\omega_j(t')\rangle=0$. The second-order coherence function with beam of Lorentzian line shape is [35]

$$\langle u(t_1)u^*(t_2)\rangle = \langle \exp i\Delta\phi\rangle = \exp\left(-\int_0^{t_1-t_2}(t_1-t_2-t)\langle\omega(t_1)\omega(t_1-t)\rangle dt\right) = \exp(-\alpha|t_1-t_2|).$$

Here, $\Delta\phi=\phi(t_1)-\phi(t_2)=\int_{t_2}^{t_1}\omega(t)dt$ has Gaussian statistics and therefore $\langle\exp i\Delta\phi\rangle=\exp(-\sigma_{\Delta\phi}^2/2)$ and by the classical relation of linear filtering, we have $\sigma_{\Delta\phi}^2=L(t_1-t_2)=2\int_0^{t_1-t_2}(t_1-t_2-t)\langle\omega(t_1)\omega(t_1-t)\rangle dt$. Now we calculate the fourth-order coherence function, which can be written as

$$\begin{aligned}\langle u_i(t_1)u_i(t_2)u_i^*(t_3)u_i^*(t_4)\rangle_{PDM} &= \exp\{-[L(t_1-t_3)+L(t_1-t_4)+L(t_2-t_3)+L(t_2-t_4)-L(t_1-t_2)-L(t_3-t_4)]\}\\ &= \exp[-\alpha_i(|t_1-t_3|+|t_1-t_4|+|t_2-t_3|+|t_2-t_4|)]\exp[\alpha_i(|t_1-t_2|+|t_3-t_4|)]\\ &= \frac{\langle u_i(t_1)u_i^*(t_3)\rangle\langle u_i(t_2)u_i^*(t_4)\rangle\langle u_i(t_1)u_i^*(t_4)\rangle\langle u_i(t_2)u_i^*(t_3)\rangle}{\langle u_i(t_1)u_i^*(t_2)\rangle\langle u_i(t_3)u_i^*(t_4)\rangle}.\end{aligned}$$

Furthermore, we have the general expression for the $2n$th-order coherence function

$$\langle u_i(t_1)\cdots u_i(t_n)u_i^*(t_{n+1})\cdots u_i^*(t_{2n})\rangle_{PDM} = \frac{\Pi_{p=1}^n\Pi_{q=1}^n\langle u_i(t_p)u_i^*(t_{n+q})\rangle}{\Pi_{p=1}^n\Pi_{q=p+1}^n\langle u_i(t_p)u_i^*(t_q)\rangle\langle u_i(t_{n+p})u_i^*(t_{n+q})\rangle}.$$

Finally, in the GAM we note that $u(t)=a(t)$, where $\varepsilon(t)$ is real and Gaussian, and fluctuates about a mean value of zero. The fourth-order coherence function of $u(t)$ satisfies [17,34]

$$\begin{aligned}\langle u_i(t_1)u_i(t_2)u_i(t_3)u_i(t_4)\rangle_{GAM} &= \langle u_i(t_1)u_i(t_3)\rangle\langle u_i(t_2)u_i(t_4)\rangle + \langle u_i(t_1)u_i(t_4)\rangle\langle u_i(t_2)u_i(t_3)\rangle + \langle u_i(t_1)u_i(t_2)\rangle\langle u_i(t_3)u_i(t_4)\rangle\\ &= \langle u_i(t_1)u_i(t_2)u_i(t_3)u_i(t_4)\rangle_{CFM} + \langle u_i(t_1)u_i(t_2)\rangle\langle u_i(t_3)u_i(t_4)\rangle\\ &= \exp[-\alpha_i(|t_1-t_3|+|t_2-t_4|)] + \exp[-\alpha_i(|t_1-t_4|+|t_2-t_3|)] + \exp[-\alpha_i(|t_1-t_2|+|t_3-t_4|)].\end{aligned}$$

In fact, according to the moment theorem for real Gaussian random variables, we have the general expression for the $2n$th-order coherence function,

$$\langle u_i(t_1)\cdots u_i(t_n)u_i(t_{n+1})\cdots u_i(t_{2n})\rangle_{GAM} = \sum_P\prod_{j\neq k'}^{2n}\langle u_i(t_1)u_i(t_k)\rangle,$$

where Σ_P indicates the summation over all possible distinct groupings of the $2n$ variables in pairs.

It will be interesting to find how the fourth-order (or higher-order) correlation functions of a color-locking field can break down to lower-order ones, which will be investigated in our future work.

A. Kerr medium with a single relaxation rate of molecular-reorientational grating

In an optical Kerr medium there is no thermal effect, we assume $\chi_T=0$. The optical Kerr effect for the liquid CS_2, for example, has at least two components, i.e., a relatively long "Debye" component and a shorter "interaction-induced" component. Here, for simplicity, we only consider the field-correlation effects in a medium which has single relaxation rate γ_M.

1. Raman-enhanced FWM

We first consider Raman-enhanced FWM. After performing the tedious integration, in the case of broadband linewidth ($\gamma_M, \gamma_R \ll \alpha_2, \alpha_3$), we obtain for $\tau>0$

$$I_A(\Delta_2,\tau) \propto \langle P_A P_A^*\rangle = L_1(n_1)\chi_M^2 + L_2\chi_R^2 - 2L_3\chi_M\chi_R, \quad (11)$$

and for $\tau<0$

$$I_A(\Delta_2,\tau) \propto L_1(n_1)\chi_M^2 + L_2\chi_R^2 - 2\left\{L_3 - \frac{4\alpha_1\gamma_R[2\alpha_3\Delta_2\cos\Delta_2\tau + (\alpha_1^2-\alpha_3^2+\Delta_2^2)\sin\Delta_2\tau]\exp(\alpha_1+\alpha_3)\tau}{\alpha_1^4 - 2\alpha_1^2(\alpha_3^2-\Delta_2^2)+(\alpha_3^2+\Delta_2^2)^2}\right\}\chi_M\chi_R. \quad (12)$$

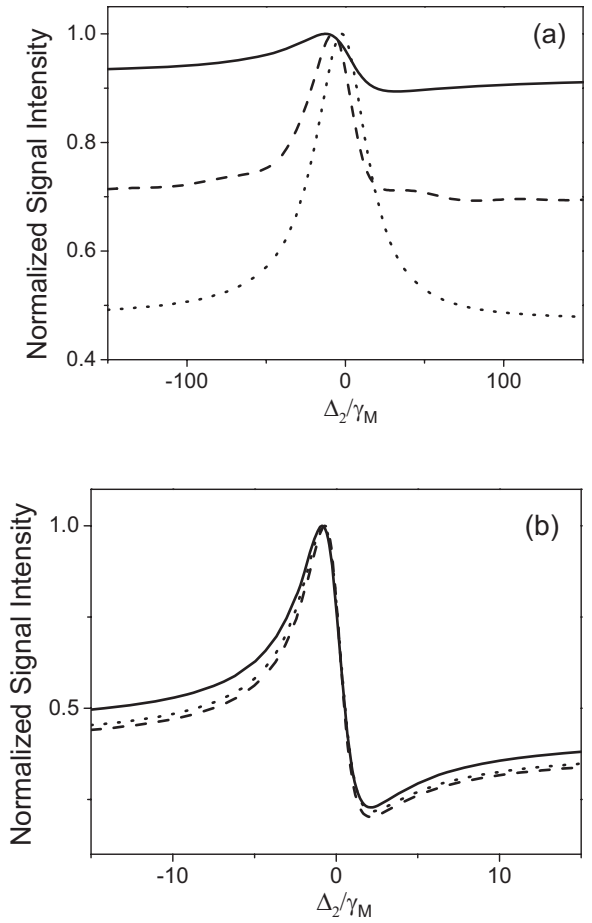

FIG. 2. Raman-enhanced FWM spectra of the GAM versus Δ_2/γ_M for $\chi_M/\chi_R=1$, $\alpha_3/\alpha_1=1$, $\alpha_1\tau=0$ (solid curve), -1 (dashed curve), -10 (dotted curve), (a) $\gamma_M/\alpha_1=0.1$, $\gamma_R/\alpha_1=0.1$, (b) $\gamma_M/\alpha_1=5$, $\gamma_R/\alpha_1=5$.

Here

$$L_1(n_1) = \gamma_M[1 + n_1 \exp(-2\alpha_1|\tau|)]/2\alpha_1 + \exp(-2\alpha_1|\tau|),$$

$$L_2 = \gamma_R(\alpha_1 + \alpha_3)/[(\alpha_1 + \alpha_3)^2 + \Delta_2^2],$$

and

$$L_3 = 2\gamma_R\Delta_2 \exp(-2\alpha_1|\tau|)/[(\alpha_1 - \alpha_3)^2 + \Delta_2^2].$$

n_1 in the function $L_1(n_1)$ equals 0, -1, 2 for the CFM, PDM, and GAM, respectively. The terms $L_1(n)\chi_M^2$ and $L_2\chi_R^2$ in Eqs. (11) and (12) are the autocorrelation terms of the nonresonant background and the resonant signal, respectively. Other terms with the factor $\chi_M\chi_R$ are the cross-correlation terms between them. Obviously, the above two equations show that the Raman-enhanced FWM spectrum is asymmetrical about $\tau=0$. Since the autocorrelation terms are the same for $\tau>0$ and $\tau<0$, the temporal asymmetry is induced by the cross-correlation terms. Moreover, when $\Delta_2\neq 0$, $I(\Delta_2,\tau)$ for $\tau<0$ exhibits hybrid-radiation-matter-detuning damping oscillations with a frequency close to Δ_2 that originate from $\cos\Delta_2\tau$ and $\sin\Delta_2\tau$ factors of interference term for $\tau<0$ [see Eq. (12) and the dashed curve in Fig. 2(a)]. On the other hand, we define a parameter $R=I(\Delta_2\to\infty)/[I(\Delta_2=0)-I(\Delta_2\to\infty)]$ as the ratio between the nonresonant background and the resonant signal. When $\tau=0$ and $\alpha_2=\alpha_3$ we obtain $R=\chi_M^2(\gamma_M+2\alpha_2)/\chi_R^2\gamma_R\gg 1$ in the limit of broadband linewidth. Thus the resonant signal at $\tau=0$ is obscured by the huge nonresonant background [the solid curve in Fig. 2(a)]. However, when $\alpha_2|\tau|\gg 1$, the resonant signal and the nonresonant background become comparable, and we have $R=\chi_M^2\gamma_M/\chi_R^2\gamma_R$, which equals 1 if $\chi_R=\chi_M$, $\gamma_R=\gamma_M$, as shown by the dashed and dotted curve in Fig. 2(a). Therefore, the huge nonresonant background can be effectively suppressed with large time delay.

Next, we consider the Raman-enhanced FWM with narrow-band linewidth ($\gamma_M,\gamma_R\gg\alpha_2,\alpha_3$). We have

$$I_A(\Delta_2) \approx n_2\left(\chi_M^2 + \chi_R^2\frac{\gamma_R^2}{\gamma_R^2+\Delta_2^2} - 2\chi_M\chi_R\frac{\gamma_R\Delta_2}{\gamma_R^2+\Delta_2^2}\right), \quad (13)$$

Here n_2 equals 2, 1, 3 for the CFM, PDM, and GAM, respectively. We can see that the autocorrelation terms are even functions while the cross-correlation term is odd function. Therefore, the spectral asymmetry of the Raman-enhanced FWM results from interference between the resonant signal and the nonresonant background (Fig. 2). Moreover, the interference term has contribution to neither the resonant signal nor nonresonant background. The ratio between the resonant signal and the nonresonant background is almost independent of the delay time τ and we have $R=(\chi_M/\chi_R)^2=1$ if $\chi_M=\chi_R$, as shown in Fig. 2(b).

In general, the Raman-enhanced FWM of Kerr medium exhibits spectral and temporal asymmetry and hybrid-radiation-matter-detuning damping oscillations with a frequency close to Δ_2 that originate from $\cos\Delta_2\tau$ and $\sin\Delta_2\tau$ factors for $\tau<0$ due to the interference between the nonresonant background of molecular-reorientation grating and the resonant signal of Raman-active mode. In addition, on one hand, in the case of narrowband linewidth the ratio between the resonant signal and the nonresonant background is almost independent of the delay time τ. On the other hand, the huge nonresonant background can be effectively suppressed with large time delay.

2. Rayleigh-enhanced FWM

Rayleigh-enhanced FWM expressions and spectra versus Δ_1/γ_M have been studied under narrowband and broadband line width conditions before [26]. In contrast to Raman-enhanced FWM, since the interference term between the molecular-reorientation grating and the Rayleigh moving grating is an even function of Δ_1, the spectra of Rayleigh-enhanced FWM are symmetrical about $\Delta_1=0$ (Fig. 3). In addition, Rayleigh moving grating does not have the exclusive relaxation rate but Debye relaxation rate γ_M instead, which is different from Raman moving grating. On the other hand, in the case of the narrowband linewidth, though the Rayleigh-enhanced FWM signal intensity of GAM is the largest while that of PDM is the smallest and that of CFM is moderate, the spectra of the three models are different drastically [Fig. 3(a)]. On the other hand, under broadband linewidth condition, when $\tau=0$, the spectra of the three models have the same point that the nonresonant background is

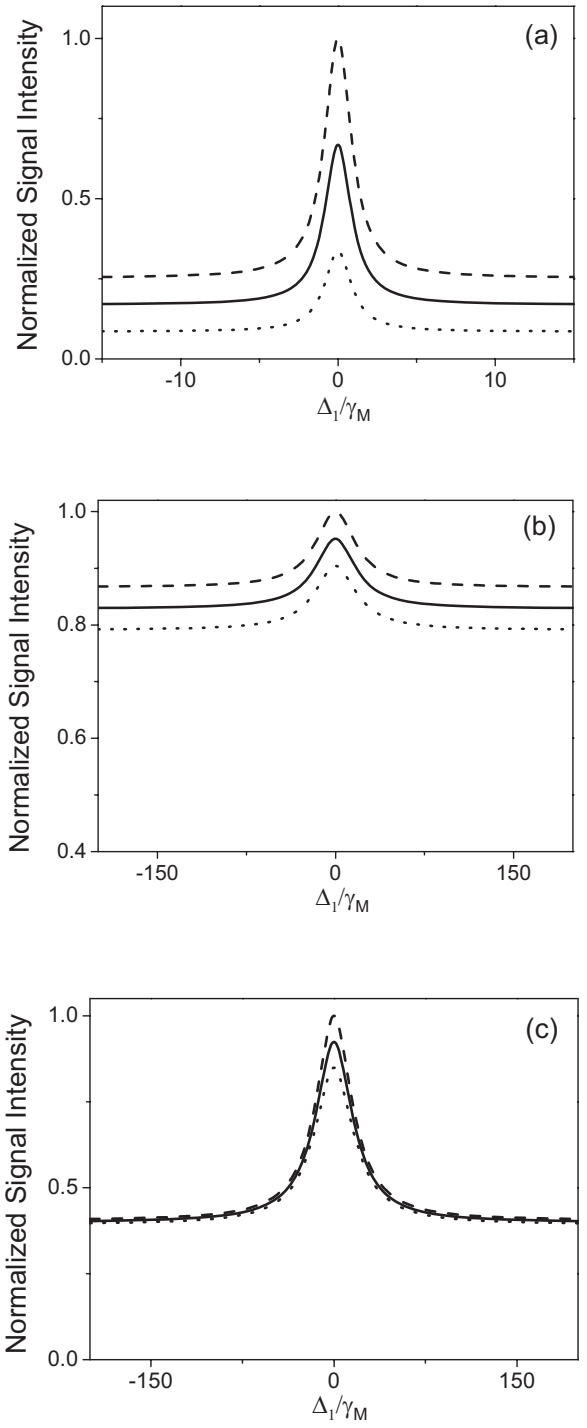

FIG. 3. Rayleigh-enhanced FWM spectra in a Kerr medium with a single relaxation rate of molecular-reorientation grating for $\alpha_3/\alpha_1=1$, (a) $\gamma_M/\alpha_1=100$, $\tau=0$; (b) $\gamma_M/\alpha_1=0.1$, $\tau=0$; (c) $\gamma_M/\alpha_1=0.1$, $\alpha_1\tau=-0.3$. The three curves represent the CFM (solid curve), PDM (dashed curve), and GAM (dotted curve), respectively.

larger than the resonant signal that the contribution from molecular-reorientation grating dominates the FWM spectra and obscure the valuable information of the spectra, the difference value of the signals intensity at $\Delta_1=0$ among the three models becomes smaller than those of Fig. 3(a), as shown in Fig. 3(b). However, when $\alpha_1\tau \gg 1$ the resonant signal and the nonresonant background become comparable and the PDM and GAM results are the same as that of the CFM, as shown in Fig. 3(c). Therefore, the differences among CFM, PDM, and GAM are drastic with narrowband linewidth, while they become similar with broadband linewidth. Also, in this case the huge nonresonant background can be effectively suppressed with large time delay.

B. Absorbing medium with the molecular-reorientation grating and the thermal grating

Typically, we assume in absorbing medium the relaxation time of a thermal grating is on the order of a microsecond, while the relaxation time of the molecular-reorientation grating is a few hundreds femtosecond, the reduction factor is about 10^{-6}. Therefore, the difference in the temporal behavior of the Raman- and Rayleigh-enhanced FWM for $\gamma_M \gg \alpha_1$, α_3 and $\gamma_T \ll \alpha_1$, α_3 can be employed for the suppression of nonresonant thermal background in an absorbing medium.

1. Raman-enhanced FWM

We have discussed the Raman-enhanced FWM spectra at fixed time delay in the Kerr medium, now we turn our attention to the dependence of the Raman-enhanced signal intensity on the time delay when the frequencies of the incident beams are fixed. Figure 4 shows the temporal behavior of the Raman-enhanced FWM signal intensity for GAM. Here no coherence spike appears at $\tau=0$ and the signal intensity decay with different rate for $\tau>0$ and $\tau<0$. In Fig. 4(a), as the laser linewidth α_2 increases, the maximum is closer to $\tau=0$, and the τ-independent background increases. Moreover, as shown in Fig. 4(b), there only exist the hybrid-radiation-matter-detuning damping oscillations for $\tau<0$ and the maximum of the profile is shifted to $\tau=0$ as Δ_2 increases. In fact, when $\tau<0$, the Raman mode and beam 1 are mutually correlated and the Raman-enhanced FWM signal intensity depends on the coherence time of the pump beams and the relaxation time of the Raman mode, while when $\tau>0$ it only depends on the laser coherence time. The temporal asymmetry and the hybrid-radiation-matter-detuning damping oscillations are induced by such mutual correlation. As the pump laser linewidth increases, the mutual correlation becomes weak and the τ-independent background increases.

For simplicity, in the limit of $\gamma_R, \gamma_M \gg \alpha_1, \alpha_3 \gg \gamma_T$ we have

$$I_A(\Delta_2,\tau) \propto [1+n_3\exp(-2\alpha_2|\tau|)] \times\left(\chi_M^2 - \frac{2\gamma_R\Delta_2}{\gamma_R^2+\Delta_2^2}\chi_M\chi_R + \frac{\gamma_R^2}{\gamma_R^2+\Delta_2^2}\chi_R^2\right) \quad (14)$$

Here n_3 equals 1, 0, 2 for CFM, PDM, and GAM, respectively. Suppose that the thermal grating is more efficient than the molecular-reorientation grating so that $\chi_T^2 \gg \chi_M^2$, χ_R^2, then we have $I_A(\Delta_2) \propto \chi_T^2$ at zero time delay. Hence, the Raman-enhanced FWM spectrum is dominated by the nonresonant thermal background, as shown in Fig. 5(a). On the other hand, under the condition $(\chi_T/\chi_M)^2(\gamma_T/2\alpha_1) \ll 1$, the thermal background can be eliminated completely when the relative time delay is much longer than the laser coherence time. In

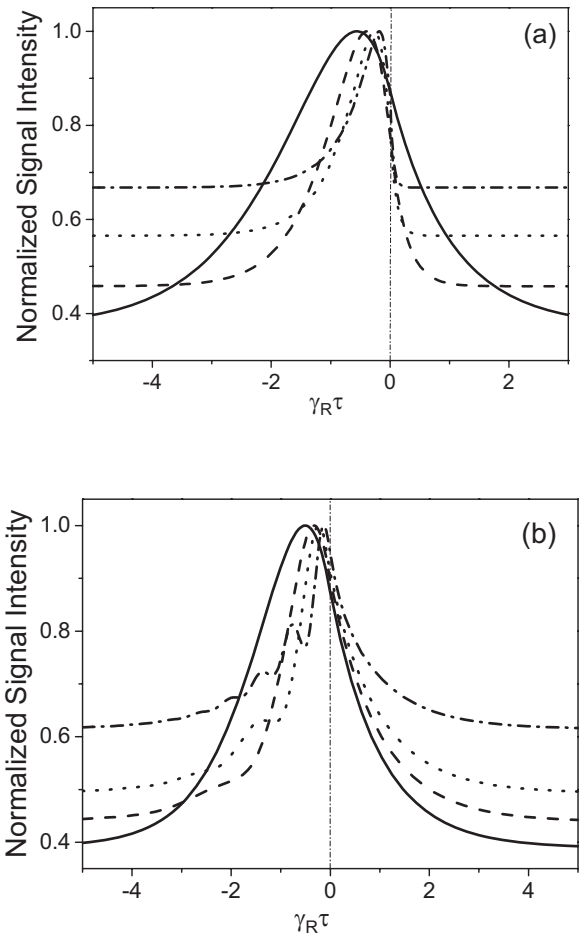

FIG. 4. Raman-enhanced FWM signal intensity of the GAM versus $\gamma_R\tau$ in an absorbing medium for (a) $\chi_M/\chi_R=0.05$, $\gamma_M/\gamma_R=4$, $\chi_T/\chi_R=0.05$, $\gamma_T/\gamma_R=1\times10^{-6}$, $\alpha_3/\gamma_R=0.1$, $\Delta_2=0$, $\alpha_2/\gamma_R=0.5$ (solid curve), $\alpha_2/\gamma_R=2$ (dashed curve), $\alpha_2/\gamma_R=5$ (dotted curve), $\alpha_2/\gamma_R=10$ (dotted-dashed curve); (b) $\chi_M/\chi_R=0.05$, $\gamma_M/\gamma_R=4$, $\chi_T/\chi_R=0.05$, $\gamma_T/\gamma_R=1\times10^{-6}$, $\alpha_3/\gamma_R=0.1$, $\alpha_2/\gamma_R=0.5$, $\Delta_2/\gamma_R=1$ (solid curve), $\Delta_2/\gamma_R=3$ (dashed curve), $\Delta_2/\gamma_R=5$ (dotted curve), $\Delta_2/\gamma_R=10$ (dotted-dashed curve).

this limit, the theoretical Raman-enhanced FWM spectra show the normal asymmetry due to the interference between the Raman-resonant term and the nonresonant background originating solely from the molecular-reorientation grating, as shown in Fig. 5(b). Furthermore, from Eq. (14) we can see that the time-delayed method to suppress the thermal background is useful for all the three Markovian stochastic models. However, if $(\chi_T/\chi_M)^2(\gamma_T/2\alpha_1)\approx1$, the residue contribution from the thermal grating due to the second term cannot be neglected even when $|\tau|\to\infty$. Our numerical results are given in Fig. 5(c).

Physically, the establishment of $Q_{M2}(\mathbf{r},t)$ and $Q_{T2}(\mathbf{r},t)$ are dependent on the delay time τ directly while that of $Q_R(\mathbf{r},t)$ is almost independent of delay time τ. Moreover, we define the coherent time of the pump beams as T_c, the decay time of the thermal grating as T_t, and the relaxation time of the molecular-reorientation grating as T_M. For most liquids T_t is of the order of microseconds, while T_M is only a few picoseconds. We choose the laser linewidth such that $T_M<T_c\ll T_t$. When $\tau\gg T_c$, the interference patterns of the pump

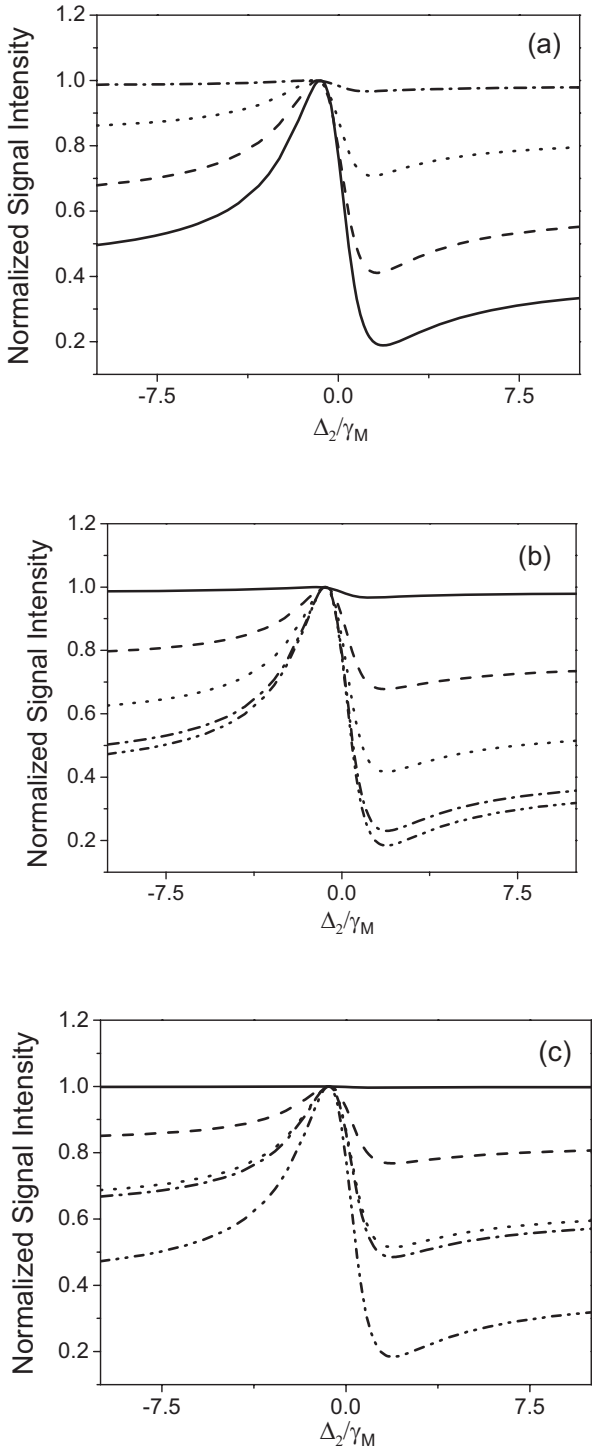

FIG. 5. Raman-enhanced FWM spectra of the GAM versus Δ_2/γ_M in an absorbing medium for (a) $\alpha_3/\alpha_1=1$, $\gamma_T/\alpha_1=1\times10^{-5}$, $\gamma_M/\alpha_1=\gamma_R/\alpha_1=10$, $\alpha_1\tau=0$, $\chi_M/\chi_R=1$, $\chi_T/\chi_R=0$ (solid curve), $\chi_T/\chi_R=1.5$ (dashed curve), $\chi_T/\chi_R=5$ (dotted curve), $\chi_T/\chi_R=50$ (dotted-dashed curve); (b) $\alpha_3/\alpha_1=1$, $\gamma_T/\alpha_1=1\times10^{-5}$, $\gamma_M/\alpha_1=\gamma_R/\alpha_1=10$, $\chi_M/\chi_R=1$, $\chi_T/\chi_R=50$, $\alpha_1\tau=0$ (solid curve), $\alpha_1\tau=3.3$ (dashed curve), $\alpha_1\tau=4$ (dotted curve), $\alpha_1\tau=5$ (dotted-dashed curve), $\chi_T/\chi_R=0$, $\alpha_1\tau=5$ (dotted-dotted-dashed curve); (c) $\alpha_3/\alpha_1=1$, $\gamma_T/\alpha_1=1\times10^{-5}$, $\gamma_M/\alpha_1=\gamma_R/\alpha_1=10$, $\chi_M/\chi_R=1$, $\chi_T/\chi_R=500$, $\alpha_1\tau=0$ (solid curve), $\alpha_1\tau=5.5$ (dashed curve), $\alpha_1\tau=7$ (dotted curve), $\alpha_1\tau=10$ (dotted-dashed curve), $\chi_T/\chi_R=0$, and $\alpha_1\tau=10$ (dotted-dotted-dashed curve).

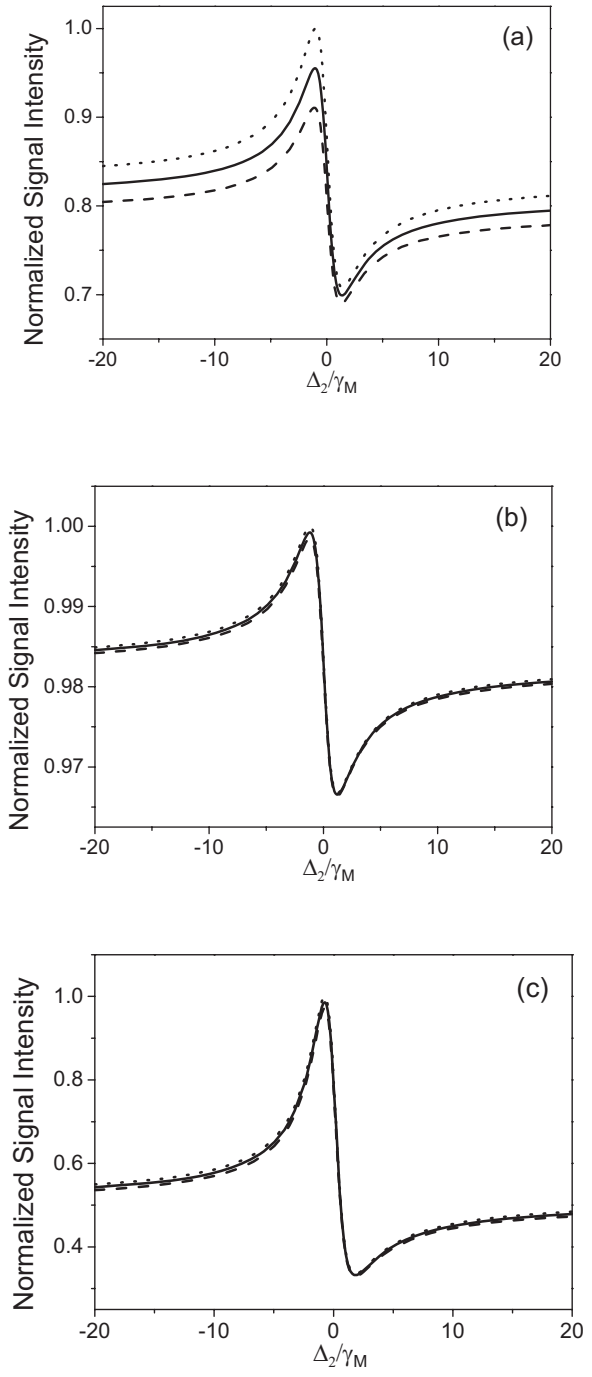

FIG. 6. Raman-enhanced FWM spectra versus Δ_2/γ_R in an absorbing medium for (a) $\gamma_M/\alpha_1=10$, $\gamma_R/\alpha_1=10$, $\gamma_T/\alpha_1=1\times10^{-5}$, $\alpha_3/\alpha_1=1$, $\chi_M/\chi_R=1$, $\chi_T/\chi_R=5$, $\tau=0$, (b) $\gamma_M/\alpha_1=10$, $\gamma_R/\alpha_1=10$, $\gamma_T/\alpha_1=1\times10^{-5}$, $\alpha_3/\alpha_1=1$, $\chi_M/\chi_R=1$, $\chi_T/\chi_R=50$, $\tau=0$, (c) $\gamma_M/\alpha_1=10$, $\gamma_R/\alpha_1=10$, $\gamma_T/\alpha_1=1\times10^{-5}$, $\alpha_3/\alpha_1=1$, $\chi_M/\chi_R=1$, $\chi_T/\chi_R=5$, $\gamma_R\tau=2$. The three curves represent the CFM (solid curve), PDM (dashed curve), and GAM (dotted curve), respectively.

beams fluctuate with a characteristic time scale $(\alpha_2+\alpha_3)^{-1}$. Thus the thermal grating is washed out due to integration effect on the phase fluctuation, while the molecular-reorientation grating with short relaxation time can respond to the phase fluctuation of the fields almost immediately. Therefore, thermal gratings can be effectively suppressed

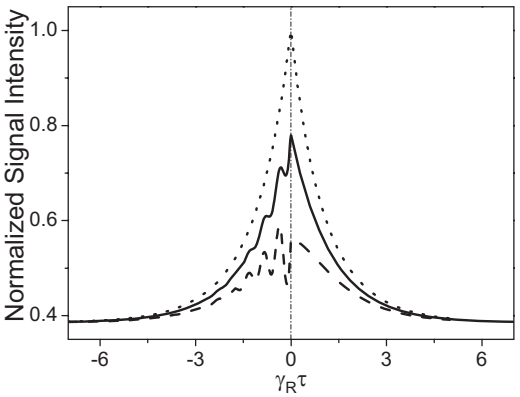

FIG. 7. Raman-enhanced FWM spectra versus $\tau\gamma_R$ for $\chi_M/\chi_R=0.05$, $\gamma_M/\gamma_R=1$, $\chi_T/\chi_R=0.1$, $\gamma_T/\gamma_R=0.000\,001$, $\alpha_3/\gamma_R=0.1$, $\alpha_1/\gamma_R=0.4$, $\Delta_2/\gamma_R=13$. The three curves represent the chaotic field (solid curve), phase-diffusion field (dashed curve), Gaussian-amplitude field (dotted curve).

with large τ, while the Bragg-reflection signal from the molecular-reorientation grating can still be observed. It should be noted that if the pump beams are derived from a pulse laser with a pulse width $T_p \ll T_t$, the condition for the suppression of thermal gratings should be replaced by $T_p \gg T_c$. That is to say, because of the finite interaction time between the laser and the material, the role of the relaxation time should be replaced by the laser pulse width.

Then we consider the difference among the three Markovian stochastic models. From Eq. (14) we can see that in the limit of γ_R, $\gamma_M \gg \alpha_1, \alpha_3 \gg \gamma_T$ PDM is short of the amplitude decay factor $\exp(-2\alpha_2\tau)$ while the amplitude decay factor of GAM is two times of that of CFM. Thus the signal intensity of GAM is largest of all and that of PDM is the smallest [Fig. 6(a)]. However, on one hand, if the thermal grating is more efficient than the molecular-reorientation grating, the same large thermal background obscures the different amplitude decay of the three models [Fig. 6(b)]. On the other hand, the difference of the three models can also be eliminated by the time delay method, as shown in Fig. 6(c) and Fig. 7.

2. Suppression of thermal background of the Rayleigh-enhanced FWM

For Rayleigh-enhanced FWM, the thermal effect of an absorbing medium can be suppressed by a time-delayed method. Physically, the resonant signal originates from the order parameters $Q_{RM}(\mathbf{r},t)$ and $Q_{RT}(\mathbf{r},t)$, while the nonresonant background come from both $Q_{M1}(\mathbf{r},t)$ and $Q_{T1}(\mathbf{r},t)$. The establishment of order parameters of the gratings involves integration effects. On the other hand, the fact that the effects of field correlation on the order parameters $Q_{RM}(\mathbf{r},t)$ $[Q_{RT}(\mathbf{r},t)]$ and $Q_{M1}(\mathbf{r},t)$ $[Q_{T1}(\mathbf{r},t)]$ are different. $Q_{RM}(\mathbf{r},t)$ $[Q_{RT}(\mathbf{r},t)]$ is induced by beams 2 and 3, the phase factor of $[E_1'(\mathbf{r},t)]^*E_3(\mathbf{r},t)$ is a random variable. Due to the integration effect, the fast random fluctuation of phase leads to the reduction of the amplitude which is almost independent of delay time τ. In contrast, since $Q_{M1}(\mathbf{r},t)$ $[Q_{T1}(\mathbf{r},t)]$ is induced by beams 1 and 2, the incident laser fields is coherent when $\tau=0$, while incoherent when $\alpha_i\tau \gg 1$, the establishment

of gratings is dependent on the delay time τ directly. In particular, we consider the condition $\gamma_M \gg \alpha_{1,3} \gg \gamma_T$. On one hand the incident fields have broadband linewidth compared to thermal grating when $\alpha_{1,3} \gg \gamma_T$. The effect of integration is to wash out the thermal grating with large time delay while no washout takes place when $\tau=0$. On the other hand the fields have narrowband linewidth compared to molecular-reorientation grating when $\gamma_M \gg \alpha_{1,3}$. In this case the material gratings have very short relaxation times and respond to the phase fluctuation of the fields almost immediately. Therefore, although the phase of P_{M1} and P_{RM} fluctuate randomly, the relative phase between them is fixed. The ratio between the nonresonant background induced by molecular-reorientation grating and the resonant signal is almost independent of τ.

IV. THE RAMAN- AND RAYLEIGH-ENHANCED NONLINEAR SUSCEPTIBILITY IN CW LIMIT

For simplicity, with cw laser beams we can assume that $u_i(t)=1$ in Eqs. (4) and (5). Under such condition the Raman-enhanced nonlinear polarization

$$P_A = P_{M2} + P_{T2} + P_R = S_2(\mathbf{r})\left(\chi_M + \chi_T - \frac{\chi_R \gamma_R}{\Delta_2 + i\gamma_R}\right) \quad (15)$$

can be obtained. Therefore, the third-order susceptibility for Raman-enhanced FWM consists of a Raman-resonant term and a nonresonant background that originates from the molecular-reorientation grating and the thermal grating, i.e.,

$$\chi_A = \chi_M + \chi_T - \frac{\chi_R \gamma_R}{\Delta_2 + i\gamma_R}. \quad (16)$$

We decompose the nonlinear susceptibility χ_A into a real and an imaginary part, i.e., $\chi_A=\chi_A'+i\chi_A''$, with $\chi_A'=\chi_M+\chi_T-\chi_R\gamma_R\Delta_2/(\Delta_2^2+\gamma_R^2)$ and $\chi_A''=\chi_R\gamma_R/(\Delta_2^2+\gamma_R^2)$. The real and imaginary parts are odd and even functions, respectively. We express χ_A as $|\chi_A|\exp i\theta_A=|\chi_A|\cos\theta_A+i|\chi_A|\sin\theta_A$, with θ_A given by $\theta_A(\Delta_2)=\tan^{-1}(\chi_A''/\chi_A')$. We can see in Fig. 8(a) the phase angle θ_A becomes more asymmetrical about $\Delta_2=0$ and the value changes more drastically when χ_M/χ_R and χ_T/χ_R decrease.

Similarly, we can obtain the Rayleigh-enhanced nonlinear polarization with cw laser beams, i.e.,

$$P_B = P_{M1} + P_{T1} + P_{RM} + P_{RT} = S_1(\mathbf{r})\left(\chi_M + \chi_T + \frac{\chi_M \gamma_M}{\gamma_M - i\Delta_1} + \frac{\chi_T \gamma_T}{\gamma_T - i\Delta_1}\right). \quad (17)$$

Therefore, the third-order susceptibility for Rayleigh-enhanced FWM consists of a Rayleigh-resonant term and a nonresonant background that originates from the molecular-reorientation grating and the thermal grating, i.e.,

$$\chi_B = \chi_M + \chi_T + \frac{\chi_M \gamma_M}{\gamma_M - i\Delta_1} + \frac{\chi_T \gamma_T}{\gamma_T - i\Delta_1}. \quad (18)$$

We decompose the nonlinear susceptibility χ_B into a real and an imaginary part, i.e., $\chi_B=\chi_B'+i\chi_B''$, with $\chi_B'=\chi_M+\chi_T+\gamma_M^2\chi_M/(\gamma_M^2+\Delta_1^2)+\gamma_T^2\chi_T/(\gamma_T^2+\Delta_1^2)$ and $\chi_B''=\chi_M\gamma_M\Delta_1/(\gamma_M^2+\Delta_1^2)+\chi_T\gamma_T\Delta_1/(\gamma_T^2+\Delta_1^2)$. In contrast of Raman-enhanced nonlinear susceptibility χ_A, the real and imaginary parts are even and odd functions, respectively. We express χ_B as $|\chi_B|\exp i\theta_B=|\chi_B|\cos\theta_B+i|\chi_B|\sin\theta_B$, with θ_B given by $\theta_B(\Delta_1)=\tan^{-1}(\chi_B''/\chi_B')$. From Fig. 8(b) we can see that $\theta_B(\Delta_1)$ is an odd function and the value changes more drastically when χ_T/χ_M decreases.

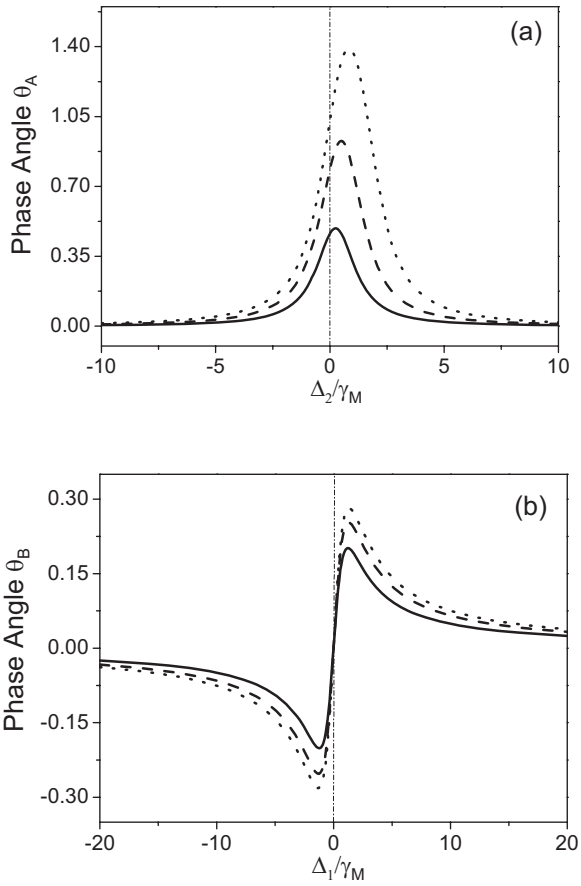

FIG. 8. (a) Phase angle θ_A versus frequency detuning Δ_2/γ_R for $\chi_M/\chi_R=\chi_T/\chi_R=1$ (solid curve), $\chi_M/\chi_R=\chi_T/\chi_R=0.5$ (dashed curve), $\chi_M/\chi_R=\chi_T/\chi_R=0.3$ (dotted curve); (b) phase angle θ_B versus frequency detuning Δ_1/γ_M for $\gamma_T/\gamma_M=1\times10^{-6}$ $\chi_T/\chi_M=1$ (solid curve), $\chi_T/\chi_M=0.5$ (dashed curve), $\chi_T/\chi_M=0.3$ (dotted curve).

V. HOMODYNE DETECTION OF ASPB

For the macroscopic system where phase matching takes place this signal must be drawn from the total third-order polarization $P^{(3)}$ developed on one chromophore multiplied by the $(P^{(3)})^*$ that is developed on another chromophore which must be located elsewhere in space (with summation over all such pairs). The bichromophoric model is particularly important to the noisy light spectroscopies where the stochastic averaging at the signal level must be carried out. The ASPB signal is proportional to the average of the absolute square of $P^{(3)}$ over the random variable of the stochastic process, so that the signal $I(\Delta_i,\tau)\propto\langle|P^{(3)}|^2\rangle=\langle P^{(3)}(P^{(3)})^*\rangle$ contains different terms in the fourth- and second-order co-

herence function of $u_i(t)$ in phase conjugation geometry. In general, the ASPB of homodyne detection (at the intensity level) can be viewed as built of the sum of three contributions: (i) the τ independent or dependent autocorrelation terms of ω_1 component, which include $u_1(t)$ fourth-order and $u_3(t)$ two-order Markovian stochastic correlation functions; (ii) the τ independent or dependent autocorrelation terms of ω_2 component, which include $u_2(t)$ fourth-order and $u_3(t)$ two-order Markovian stochastic correlation functions; (iii) the τ-dependent cross-correlation terms between ω_1 and ω_2 components, which include $u_1(t)$, $u_2(t)$, and $u_3(t)$ second-order Markovian stochastic correlation functions. Different Markovian stochastic models of the laser field only affect the fourth-order, not second-order correlation functions.

A. Raman ASPB

For the Raman ASPB, we have the total third-order polarization $P^{(3)}=P_A+P_D=(P_{M2}+P_{T2}+P_R)+(P_{M1}+P_{T1})$. Therefore, the homodyne-detection signal $I(\Delta_2,\tau)$ contains $5\times5=25$ different terms which include the nonresonant terms of the ω_1 molecular- reorientation and thermal gratings, terms of the ω_2 molecular-reorientation and thermal gratings and Raman resonant mode, and the cross-correlation terms between FWM and Raman-enhanced FWM.

The composite noisy beam 1 (beam 2) is treated as one whose spectrum is simply a sum of two Lorentzians. The high-order decay cross-correlation terms are reasonably neglected in our treatment. After performing the tedious integration from Eqs. (4)–(8), in the limit $\gamma_M,\gamma_R \gg \alpha_1,\alpha_2,\alpha_3 \gg \gamma_T$ we obtain

$$\begin{aligned} I_{ASPB}(\Delta_2,\tau) \propto \eta^2 \exp(-2i\Delta\mathbf{k}\cdot\mathbf{r})\{[1+n_4\exp(-2\alpha_2|\tau|)]L_5 \\ + L_6\} + \{[1+n_4\exp(-2\alpha_1|\tau|)]\times\chi_M^2 + L_7\} \\ + \eta L_8\{\exp[i\Delta\mathbf{k}\cdot\mathbf{r} - i(\omega_1+\omega_2)|\tau|]\chi_A^* \\ + \exp[-i\Delta\mathbf{k}\cdot\mathbf{r} + i(\omega_1+\omega_2)|\tau|]\chi_A\}. \end{aligned} \tag{19}$$

Here

$$L_5 = \chi_M^2 - 2\gamma_R\Delta_2\chi_M\chi_R/(\gamma_R^2+\Delta_2^2) + \gamma_R^2\chi_R^2/(\gamma_R^2+\Delta_2^2),$$

$$L_6 = \exp(-2\alpha_2|\tau|)[2\chi_M\chi_T - 2\gamma_R\Delta_2\chi_T\chi_R/(\gamma_R^2+\Delta_2^2) + \chi_T^2],$$

$$L_7 = \exp(-2\alpha_1|\tau|)(2\chi_M\chi_T + \chi_T^2),$$

$$L_8 = (\chi_M+\chi_T)\exp[-(\alpha_1+\alpha_2)|\tau|],$$

$$\chi_A = \chi_M + \chi_T - \chi_R\gamma_R/(\Delta_2 + i\gamma_R),$$

$$\eta = \varepsilon_2'(\varepsilon_2)^*/\varepsilon_1(\varepsilon_1')^*,$$

$$\Delta\mathbf{k} = (\mathbf{k}_1-\mathbf{k}_1') - (\mathbf{k}_2'-\mathbf{k}_2),$$

and n_4 equals 1, 0, 2 for the CFM, PDM, and GAM, respectively.

First for CFM, the Raman ASPB versus τ shows the attosecond scale modulation with a sum frequency $\omega_1+\omega_2$ and damping rates α_1 and α_2 (see Fig. 9). The constant term $\gamma_R^2\chi_R^2/(\gamma_R^2+\Delta_2^2)$ in Eq. (16), which is independent of the relative time delay between twin beams 1 and 2, originates from the phase fluctuation of the chaotic fields, while the purely decay terms including these factors $\exp(-2\alpha_1|\tau|)$, $\exp(-2\alpha_2|\tau|)$ come from amplitude fluctuation of the chaotic fields.

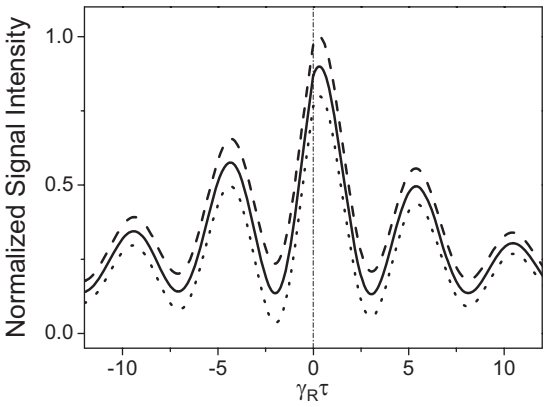

FIG. 9. The Raman ASPB signal intensity versus $\gamma_R\tau$ for $\chi_M/\chi_R=0.2$, $\gamma_M/\gamma_R=1$, $\chi_T/\chi_R=1$, $\gamma_T/\gamma_R=1\times10^{-6}$, $\alpha_2/\gamma_R=0.05$, $\alpha_1/\gamma_R=\alpha_3/\gamma_R=0.1$, $\Delta_2=0$, $r=0$, $\omega_1/\alpha_2=11.99$, $\omega_2/\alpha_2=12.75$, and $\eta=1$. The three curves represent the chaotic field (solid curve), Gaussian-amplitude field (dashed curve), and phase-diffusion field (dotted curve).

Secondary for PDM the temporal behavior of the beat signal only reflects the characteristic of the lasers. The result is remarkably different from that based on a chaotic model. It is short of the purely autocorrelation decay terms including these factors $\exp(-2\alpha_1|\tau|)$ and $\exp(-2\alpha_2|\tau|)$, which are shown to be particularly insensitive to the phase fluctuation of the Markovian stochastic light fields. The drastic difference of the results also exists in the higher-order correlation on Rayleigh ASPB when three Markovian stochastic models are employed [26].

Third for GAM, in contrast to CFM and PDM, the decay term includes the factors $2\exp(-2\alpha_1|\tau|)$ and $2\exp(-2\alpha_2|\tau|)$. The τ-dependent term of Gaussian-amplitude field is larger than that of the chaotic field and the phase-diffusion field (Fig. 9), which originates from the amplitude fluctuation of the Markovian stochastic field. The physical explanation for this is that the Gaussian-amplitude field undergoes stronger intensity fluctuations than a chaotic field. On the other hand, the intensity (amplitude) fluctuations of the Gaussian-amplitude field or the chaotic field are always much larger than the pure phase fluctuations of the phase-diffusion field.

B. Rayleigh ASPB

For the Rayleigh ASPB, we have the total third-order polarization $P^{(3)}=P_B+P_C=(P_{M1}+P_{RM}+P_{T1}+P_{RT})+(P_{M2}+P_{T2})$. Therefore, the homodyne-detection signal $I(\Delta_1,\tau)$ contains $6\times6=36$ different terms which include the nonresonant terms of the ω_2 molecular-reorientation and thermal gratings, terms of the ω_1 molecular-reorientation and thermal gratings and Rayleigh resonant mode, and the cross-correlation terms between FWM and Rayleigh-enhanced FWM.

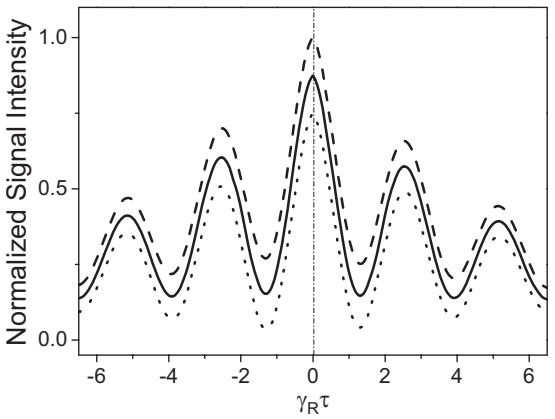

FIG. 10. The Rayleigh ASPB signal intensity versus $\gamma_M\tau$ for $\chi_M/\chi_T=1$, $\gamma_T/\gamma_M=1\times10^{-6}$, $\alpha_1/\gamma_M=\alpha_2/\gamma_M=\alpha_3/\gamma_M=0.1$, $\Delta_1=0$, $r=0$, $\omega_1/\alpha_1=12.08$, $\omega_2/\alpha_1=11.99$, and $\eta=1$. The three curves represent the chaotic field (solid curve), Gaussian-amplitude field (dashed curve), and phase-diffusion field (dotted curve).

After performing the tedious integration of Eqs. (4)–(7), (9), and (10), in the limit $\gamma_M,\gamma_R\gg\alpha_1,\alpha_2,\alpha_3\gg\gamma_T$ we obtain

$$I_{ASPB}(\Delta_1,\tau)\propto\{[1+n_4\exp(-2\alpha_1|\tau|)]L_9+L_{10}\}+\eta^2\exp(-2i\Delta\mathbf{k}\cdot\mathbf{r})\{[1+n_4\exp(-2\alpha_2|\tau|)]\chi_M^2+L_{11}\}+\eta L_8\{\exp[i\Delta\mathbf{k}\cdot\mathbf{r}-i(\omega_1+\omega_2)|\tau|]\chi_B+\exp[-i\Delta\mathbf{k}\cdot\mathbf{r}+i(\omega_1+\omega_2)|\tau|]\chi_B^*\}. \quad (20)$$

Here, $L_9=[1+3\gamma_M^2/(\gamma_M^2+\Delta_1^2)]\chi_M^2$, $L_{10}=\exp(-2\alpha_1|\tau|)\times\{[1+\gamma_M^2/(\gamma_M^2+\Delta_1^2)]2\chi_M\chi_T+\chi_T^2\}$, $L_{11}=\exp(-2\alpha_2|\tau|)\times(2\chi_M\chi_T+\chi_T^2)$, and $\chi_B=\chi_M+\chi_T+\chi_M\gamma_M/(\gamma_M-i\Delta_1)$.

Similarly with Raman ASPB, first for CFM, under such condition the Rayleigh ASPB shows the attosecond scale modulation with a sum frequency $\omega_1+\omega_2$ and damping rates α_1 and α_2 (see Fig. 10). On the other hand, since Rayleigh-enhanced FWM exhibits spectral symmetry, which is different from Raman-enhanced FWM, Eq. (20) also shows symmetry about Δ_1.

Similarly, secondary for PDM, Eq. (20) of PDM is insensitive to the intensity fluctuation (amplitude fluctuation) and is short of decay terms $\exp(-2\alpha_1|\tau|)$ and $\exp(-2\alpha_2|\tau|)$, which is remarkably different from the result based on a chaotic model. It indicates that the τ-independent term $3\gamma_M^2/(\gamma_M^2+\Delta_1^2)$ comes from the phase fluctuation.

Third for GAM due to the amplitude fluctuation of the Markovian stochastic field, Rayleigh ASPB of GAM has the τ-dependent factors $2\exp(-2\alpha_1|\tau|)$ and $2\exp(-2\alpha_2|\tau|)$, which is larger than that of CFM and PDM.

We find that as the Rayleigh-mode detuning $\Delta_1=0$, the temporal behavior of the Rayleigh ASPB is symmetric with the maximum of the beat signal at $\tau=0$ (Fig. 10), while as the Raman-mode detuning $\Delta_2=0$, that of the Raman ASPB is asymmetric with the maximum of the beat signal shifted from $\tau=0$ (Fig. 9). In fact it is induced by phase shift of Raman phase-angle θ_A and Rayleigh phase-angle θ_B, respectively. When $\Delta_1=\Delta_2=0$, we have $\theta_A\neq0$ and $\theta_B=0$, as shown in Figs. 8(a) and 8(b), respectively.

C. Coexisting of Raman and Rayleigh ASPB

For the coexisting of Raman and Rayleigh ASPB, we have the total third-order polarization $P^{(3)}=P_A+P_B=P_{M2}+P_{T2}+P_R+P_{M1}+P_{RM}+P_{T1}+P_{RT}$. Therefore, the homodyne-detection signal $I(\Delta_1,\tau)\propto\langle(P_A+P_B)(P_A^*+P_B^*)\rangle$ contains $7\times7=49$ different terms which include the terms of the ω_2 molecular reorientation and thermal gratings and Raman resonant mode, the terms of the ω_1 molecular reorientation and thermal gratings and Rayleigh resonant mode, and the cross-correlation terms between Raman-enhanced and Rayleigh-enhanced FWM.

By virtue of the result of the integration in pure Raman and pure Rayleigh ASPB shown above, in the limit $\gamma_M,\gamma_R\gg\alpha_1,\alpha_2,\alpha_3\gg\gamma_T$ we obtain

$$I_{ASPB}(\Delta_1,\Delta_2,\tau)\propto\eta^2\exp(-2i\Delta\mathbf{k}\cdot\mathbf{r})\{[1+n_4\exp(-2\alpha_2|\tau|)]L_5+L_6\}+\{[1+n_4\exp(-2\alpha_1|\tau|)]\times L_9+L_{10}\}+\eta\exp[-(\alpha_1+\alpha_2)|\tau|]\{\exp[i\Delta\mathbf{k}\cdot\mathbf{r}-i(\omega_1+\omega_2)|\tau|]\chi_A^*\chi_B+\exp[-i\Delta\mathbf{k}\cdot\mathbf{r}+i(\omega_1+\omega_2)\times|\tau|]\chi_A\chi_B^*\}. \quad (21)$$

First for CFM, we can see that Raman- and Rayleigh-enhanced FWM autocorrelation terms coexist and they interfere with each other and generate ASPB. The autocorrelation terms decay with a time constant α_1^{-1} and α_2^{-1} while the cross-correlation term is modulated with a sum frequency $\omega_1+\omega_2$ and a damping rate $\alpha_1+\alpha_2$. The interferometric contrast ratio of interferogram mainly determined the cross correlation between Raman- and Rayleigh-enhanced FWM processes is equally sensitive to the amplitude and phase fluctuations of the chaotic fields. Physically, the chaotic field has the property of photon bunching, which can affect any multiphoton process when the higher-order correlation function of the field plays an important role.

Secondary for PDM, in the case of $\gamma_M\gg\alpha_1,\alpha_2,\alpha_3\gg\gamma_T$ of PDM, both the Raman- and Rayleigh-enhanced FWM autocorrelation terms in Eq. (21) are short of the purely decay factors $\exp(-2\alpha_1|\tau|)$ and $\exp(-2\alpha_2|\tau|)$. The phase-diffusion model predicts the ASPB signal has a damping oscillation of the attosecond sum frequency around a constant value (Fig. 11). We can understand this phenomenon as follows. The interference pattern of the ω_1 (ω_2) component of the twin composite beams 1 and 2 will be in constant motion with a characteristic time constant α_1^{-1} (α_2^{-1}) when $|\tau|$ is much longer than the laser coherence time τ_c. On the other hand, the relaxation time of the molecular-reorientation grating is so short that the induced gratings G_{M1} (G_{T1},G_{RM},G_{RT}) and G_{M2} (G_{T2},G_R) always follow the interference pattern, and therefore the beat signal will never decay. Furthermore, the relative phase between G_{M1} (G_{T1},G_{RM},G_{RT}) and G_{M2} (G_{T2},G_R) fluctuates randomly, which makes spatial interference between them impossible. In this case the beat signal intensity is simply the summation of the signal intensity originating from G_{M1} (G_{T1},G_{RM},G_{RT}) and G_{M2} (G_{T2},G_R). In contrast, the fringes of G_{M1} (G_{T1},G_{RM},G_{RT}) and G_{M2} (G_{T2},G_R) are stable when $|\tau|<\tau_c$. The constructive or destructive interference between G_{M1} (G_{T1},G_{RM},G_{RT}) and G_{M2}

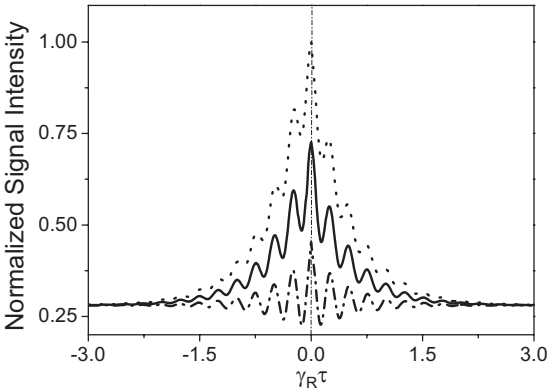

FIG. 11. The coexisting of Raman and Rayleigh ASPB signal intensity versus $\alpha_1\tau$ for $\chi_M/\chi_R=10$, $\gamma_M/\alpha_1=\gamma_R/\alpha_1=10$, $\chi_T/\chi_R=1$, $\gamma_T/\alpha_1=1\times10^{-5}$, $\alpha_2/\alpha_1=\alpha_3/\alpha_1=1$, $\Delta_1=\Delta_2=0$, $r=0$, $\omega_1/\alpha_1=12.08$, and $\omega_2/\alpha_1=12.75$, $\eta=0.3$. The three curves represent the chaotic field (solid curve), Gaussian-amplitude field (dotted curve), and phase-diffusion field (dotted-dashed curve).

(G_{T2},G_R) enhances or reduces the beat signal and gives rise to the oscillation of the beat signal intensity as τ varies. We note that the main difference between the phase-diffusion model and the chaotic model is that amplitude fluctuation exists in the latter case. When $|\tau|<\tau_c$, the coincidence of the intensity spikes of the two composite beams gives an additional enhancement of the beat signal for the chaotic model (Fig. 11).

Third for GAM, apparently, the τ-dependent term $2\exp(-2\alpha_1|\tau|)$ and $2\exp(-2\alpha_2|\tau|)$ of Gaussian-amplitude field is larger than that of the chaotic field and the phase-diffusion field and the signal intensity of $\tau=0$ for GAM is largest of three models (Fig. 11). However, Eq. (21) shows that the τ-independent terms of three models are the same and do not include the factor χ_T. On the other hand, though the polarization beat signal is shown to be particularly sensitive to the statistical properties of the Markovian stochastic light fields with arbitrary bandwidth, different Markovian stochastic models of the laser field only affect the fourth-, not second-order correlation functions. The cross-correlation terms between Raman- and Rayleigh-enhanced polarization of three models are the same. Therefore, Fig. 11 shows that ASPB signal intensities in CFM, PDM, and GAM versus τ oscillate with the same frequency $\omega_1+\omega_2$ and have the same background.

Next, we discuss the chromophore $P^{(3)}$ difference between the ASPB with a phase-conjugation geometry and the sum-frequency UMS [1] with a self-diffraction geometry from a physical viewpoint. The frequencies and wave vectors of the sum-frequency UMS signal are $\omega_A=2\omega_2-\omega_2$, $\omega_B=2\omega_1-\omega_1$, and $k_A=2k_2-k'_2$, $k_B=2k'_1-k_1$, respectively, which means that a photon is absorbed from each of the two mutually correlated fluctuating pump beams. On the other hand, the frequencies and wave vectors of the ASPB signal are $\omega_A=\omega_2-\omega_2+\omega_3$, $\omega_B=\omega_1-\omega_1+\omega_3$ and $\mathbf{k}_A=\mathbf{k}_1-\mathbf{k}'_1+\mathbf{k}_3$, $\mathbf{k}_B=\mathbf{k}'_2-\mathbf{k}_2+\mathbf{k}_3$, respectively (Fig. 1), therefore photons are absorbed from and emitted to the mutually correlated fluctuating twin beams 1 and 2, respectively. This difference between ASPB and UMS has profound influence on the field-correlation effects. We note that the role of beams 1 and 2 are interchangeable in the UMS, this interchangeable feature also makes the second-order coherence function theory failure in the UMS. Due to $\langle u(t_1)u(t_2)\rangle=0$, the absolute square of the stochastic average of the polarization $|\langle P^{(3)}\rangle|^2$ cannot be used to describe the temporal behavior of the sum-frequency UMS [1]. Our higher-order correlation (intensity correlation) treatment also is of vital importance in the sum-frequency UMS. Moreover, because of $\langle u_i(t)\rangle=0$ and $\langle u_i^*(t)\rangle=0$, the absolute square of the stochastic average of the polarization $|\langle P^{(3)}\rangle|^2$, which involves second-order coherence function of $u_i(t)$, cannot be used to describe the temporal behavior of the ASPB. The sixth-order correlation theory $\langle|P^{(3)}|^2\rangle$ reduces to the second-order correlation theory $|\langle P^{(3)}\rangle|^2$ in the case that the laser pulse width is much longer than the laser coherence time. The second-order coherence function theory is valid when we are only interested in the τ-dependent part of the beating signal [13]. Therefore, the fourth-order coherence function theory is of vital importance in ASPB. The application of higher-order results to the difference-frequency polarization beat experiment yielded a better fit to the data than an expression involving only second-order coherence [13,29–33,36]. Apparently the nature of the Markovian field has a more drastic effect on the outcome of the experiment than the underlying molecular nonlinearity. Since real laser fields are unlikely to behave similar to the pure three field classes, a complicated superposition of various types of responses is to be expected.

VI. HETERODYNE DETECTION OF ASPB

Since optical fields oscillate too quickly for direct detection they must be measured "in quadrature"—as photons. One common measurement technique, such as FWM measured at its quadrature $I_A=P_AP_A^*$ or $I_B=P_BP_B^*$, yields only absolute values of the nonlinear susceptibility $|\chi_A|^2$ or $|\chi_B|^2$. Thus, all phase information in the nonlinear susceptibility is lost. The second way to achieve quadrature is the phase-sensitive method used for optical heterodyne detection. We introduce another reference FWM signal designed in frequency and wave vector (Fig. 1) to conjugate (go into quadrature) in its complex representation with the new polarization of interest. Both the measured signal and the reference signal have the same frequency, thus, they interfere directly at the detector and generate ASPB by changing the relative time delay τ between the measured beam and the reference beam. In other words the total signal is modulated by the time delay. In the heterodyne case that the reference signal is larger than the measured signal, the phase information is retained and one can take a full measure of the complex susceptibility through adjusting the time delay τ. The phase of the complex induced polarization determines how its energy will partition between class I (the absorbed or emitted active spectroscopy) and class II (the passive spectroscopy with a new launched field) spectroscopy [2–9,36–38].

A. Raman ASPB

For the Raman-enhanced FWM signal with polarization P_A, we introduce the reference FWM signal with polarization

P_D. Thus the Raman ASPB signal is proportional to the average of the absolute square of P_A+P_D over the random variable of the stochastic process, so that the signal intensity $I(\Delta_2,\tau)\propto\langle|P_A+P_D|^2\rangle=\langle(P_A+P_D)(P_A^*+P_D^*)\rangle$ $=\langle P_AP_A^*\rangle+\langle P_DP_D^*\rangle+\langle P_AP_D^*\rangle+\langle P_DP_A^*\rangle$ contains $5\times5=25$ different terms in the fourth- and second-order coherence function of $u_i(t)$ in phase conjugation geometry. In general, the Raman ASPB (at the intensity level) can be viewed as built of the sum of three contributions: (i) the τ-independent or -dependent autocorrelation terms $I_A(\Delta_2,\tau)=\langle P_AP_A^*\rangle$ (i.e., Raman-enhanced FWM) of ω_2 nonresonant molecular reorientation and thermal gratings, and Δ_2 Raman resonant mode, which include the $u_2(t)$ fourth-order and the $u_3(t)$ second-order Markovian stochastic correlation functions; (ii) the τ-independent or -dependent nonresonant autocorrelation terms $I_D(\tau)=\langle P_DP_D^*\rangle$ of ω_1 molecular reorientation and thermal gratings, which include $u_1(t)$ fourth-order and $u_3(t)$ second-order Markovian stochastic correlation functions; (iii) the τ-dependent cross-correlation terms $I_{A,D}(\Delta_2,\tau)$ $=\langle P_AP_D^*\rangle+\langle P_DP_A^*\rangle$ between Raman-enhanced FWM and nondegenerate FWM (NDFWM) processes, which include $u_1(t)$, $u_2(t)$, and $u_3(t)$ second-order Markovian stochastic correlation functions. Different Markovian stochastic models of the laser field only affect the fourth-, not second-order correlation functions. Therefore, the cross-correlation terms are the same for three Markovian stochastic models. Furthermore, by virtue of the cross-correlation term $I_{A,D}(\Delta_2,\tau)$ we can obtain the third-order susceptibilities for the Raman-enhanced FWM $\chi_A=\chi_M+\chi_T-\chi_R\gamma_R/[\Delta_2+i(\alpha_2+\alpha_3+\gamma_R)]$ and for the reference NDFWM $\chi_D=\chi_M+\chi_T$ theoretically. The real and imaginary parts of χ_A are odd and even functions, i.e., $\chi'_A=\chi_M+\chi_T-\chi_R\gamma_R\Delta_2/[\Delta_2^2+(\alpha_2+\alpha_3+\gamma_R)^2]$ and $\chi''_A=\chi_R\gamma_R(\alpha_2+\alpha_3+\gamma_R)/[\Delta_2^2+(\alpha_2+\alpha_3+\gamma_R)^2]$, respectively.

In heterodyne detection, we assume $I_D(\tau)\gg I_A(\Delta_2,\tau)$ that at intensity level, in other words, we let $\eta\ll1$, thus we have $I\propto I_D(\tau)+I_{A,D}(\Delta_2,\tau)$. For simplicity, in the limit of $\gamma_R,\gamma_M\gg\alpha_1,\alpha_2,\alpha_3\gg\gamma_T$ and based on the chaotic, the phase-diffusion, and the real Gaussian fields, we have the Raman ASPB signals, respectively, i.e.,

$$\begin{aligned}I_{ASPB}(\Delta_2,\tau)\propto&\{[1+n_4\exp(-2\alpha_1|\tau|)]\chi_M^2+L_7\}\\&+\eta L_8\{\exp[i\Delta\mathbf{k}\cdot\mathbf{r}-i(\omega_1+\omega_2)|\tau|]\chi_A^*\\&+\exp[-i\Delta\mathbf{k}\cdot\mathbf{r}+i(\omega_1+\omega_2)|\tau|]\chi_A\}.\end{aligned}\quad(22)$$

We express χ_A as $|\chi_A|\exp(i\theta_A)=|\chi_A|\cos\theta_A+i|\chi_A|\sin\theta_A$, with θ_A (Fig. 8). Therefore, we have

$$\begin{aligned}I_{ASPB}(\Delta_2,\tau)\propto&I_D(\tau)+2L_8\eta|\chi_A|\cos[-\Delta\mathbf{k}\cdot\mathbf{r}+(\omega_1+\omega_2)|\tau|\\&+\theta_A].\end{aligned}\quad(23)$$

Equation (23) indicates that the reference FWM signal $I_D(\tau)$ and the factor $2L_8\eta$ are independent of Δ_2, while the heterodyne signal is modulated with a sum frequency $\omega_1+\omega_2$ as τ is varied, in addition, the phase of the oscillation depends on the phase θ_A of the measured third-order susceptibility χ_A. If we adjust the time delay τ such that $-\Delta\mathbf{k}\cdot\mathbf{r}+(\omega_1+\omega_2)|\tau|=2n\pi$, then

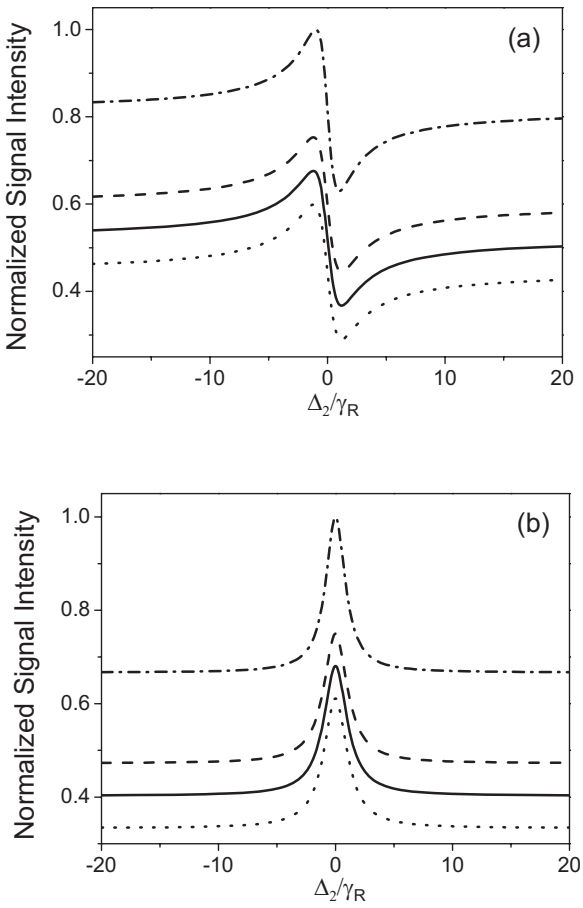

FIG. 12. The heterodyne detection spectra versus Δ_2/γ_R of the Raman ASPB with (a) $\tau=(-2\pi+\Delta\mathbf{k}\cdot\mathbf{r})/(\omega_1+\omega_2)$ for the real part of χ_A, while with (b) $\tau=(-2\pi+\pi/2+\Delta\mathbf{k}\cdot\mathbf{r})/(\omega_1+\omega_2)$ for the imaginary part of χ_A. The other parameters are for $\chi_M/\chi_R=0.1$, $\gamma_M/\alpha_1=\gamma_R/\alpha_1=10$, $\chi_T/\chi_R=0.1$, $\gamma_T/\alpha_1=1\times10^{-5}$, $\alpha_2/\alpha_1=\alpha_3/\alpha_1=1$, $\eta=0.1$. Theoretical curves are shown in CFM (solid curve), PDM (dotted curve), GAM (dashed curve), and the model with cw laser beams (dotted-dashed curve).

$$I_{ASPB}(\Delta_2,\tau)\propto I_D(\tau)+2L_8\eta|\chi_A|\cos\theta_A\propto I_D(\tau)+2L_4\eta\chi'_A.\quad(24)$$

However, if $-\Delta\mathbf{k}\cdot\mathbf{r}+(\omega_1+\omega_2)|\tau|=(2n-1/2)\pi$, we have

$$I_{ASPB}(\Delta_2,\tau)\propto I_D(\tau)+2L_8\eta|\chi_A|\sin\theta_A\propto I_D(\tau)+2L_4\eta\chi''_A.\quad(25)$$

In other words, by changing the time delay τ between beams 1 and 2 we can obtain the real and the imaginary parts of the Raman-enhanced susceptibility χ_A.

Figure 12 shows the heterodyne detection spectra versus Δ_2/γ_R of the Raman ASPB. We can see that the spectra have the profile of the real and imaginary parts of the Raman resonance with comparable backgrounds. On the other hand, in Fig. 12 the spectra of CFM, PDM, and GAM are the same as those of cw beam. However, the background of the three Markovian models is smaller than that of the cw beam due to the phase fluctuation.

B. Rayleigh ASPB

For the Rayleigh-enhanced FWM signal with polarization P_B, we introduce the reference FWM signal with polarization P_C. Thus the Rayleigh ASPB signal is proportional to the average of the absolute square of P_B+P_C, so that the signal intensity $I(\Delta_1,\tau)\propto\langle|P_B+P_C|^2\rangle=\langle(P_B+P_C)(P_B^*+P_C^*)\rangle$ contains $6\times6=36$ different terms where $I_B(\Delta_1,\tau)=\langle P_BP_B^*\rangle$ and $I_C(\tau)=\langle P_CP_C^*\rangle$ include the $u_1(t)$ and the $u_2(t)$ fourth-order Markovian stochastic correlation functions, respectively, while $I_{B,C}(\Delta_1,\tau)=\langle P_BP_C^*\rangle+\langle P_BP_C^*\rangle$ include $u_i(t)$ second-order Markovian stochastic correlation functions. We know that different Markovian stochastic models of the laser field only affect the fourth-, not second-order correlation functions. Therefore, the cross-correlation terms $I_{B,C}(\Delta_1,\tau)$ are the same for three Markovian stochastic models, from which we can obtain the third-order susceptibilities for the Rayleigh-enhanced FWM $\chi_B=\chi_M+\chi_T+\chi_M\gamma_M/[(\alpha_1+\alpha_3+\gamma_M)-i\Delta_1]+\chi_T\gamma_T/[(\alpha_1+\alpha_3+\gamma_T)-i\Delta_1]$ and for the reference NDFWM $\chi_C=\chi_M+\chi_T$ theoretically. The real and imaginary parts of χ_B are even and odd functions, i.e.,

$$\chi_B'=\chi_M+\chi_T+\gamma_M(\alpha_1+\alpha_3+\gamma_M)\chi_M/[(\alpha_1+\alpha_3+\gamma_M)^2+\Delta_1^2]+\gamma_T(\alpha_1+\alpha_3+\gamma_T)\chi_T/[(\alpha_1+\alpha_3+\gamma_T)^2+\Delta_1^2],$$

$$\chi_B''=\chi_M\gamma_M\Delta_1/[(\alpha_1+\alpha_3+\gamma_M)^2+\Delta_1^2]+\chi_T\gamma_T\Delta_1/[(\alpha_1+\alpha_3+\gamma_T)^2+\Delta_1^2],$$

respectively.

In heterodyne detection, we assume $I_C(\tau)\gg I_B(\Delta_1,\tau)$ at intensity level, in other words, we let $\eta\gg1$, thus we have $I(\Delta_1,\tau)\propto I_C(\tau)+I_{B,C}(\Delta_1,\tau)$. Under the condition of $\gamma_M\gg\alpha_1,\alpha_2,\alpha_3\gg\gamma_T$ we have the Rayleigh ASPB signals for the three Markovian models, respectively, i.e.,

$$I_{ASPB}(\Delta_1,\tau)\propto\eta^2\exp(-2i\Delta\mathbf{k}\cdot\mathbf{r})\{[1+n_4\exp(-2\alpha_2|\tau|)]\chi_M^2+L_{11}\}+\eta L_8\{\exp[i\Delta\mathbf{k}\cdot\mathbf{r}-i(\omega_1+\omega_2)|\tau|]\chi_B+\exp[-i\Delta\mathbf{k}\cdot\mathbf{r}+i(\omega_1+\omega_2)|\tau|]\chi_B^*\}. \quad (26)$$

We express χ_B as $|\chi_B|\exp(i\theta_B)=|\chi_B|\cos\theta_B+i|\chi_B|\sin\theta_B$, with θ_B (Fig. 9). From Eq. (26) we have

$$I_{ASPB}(\Delta_1,\tau)\propto I_C(\tau)+2L_8\eta|\chi_B|\cos[\Delta\mathbf{k}\cdot\mathbf{r}-(\omega_1+\omega_2)|\tau|+\theta_B]. \quad (27)$$

Equation (27) indicates that the reference FWM signal $I_C(\tau)$ and the factor $2L_8\eta$ are independent of Δ_1. The heterodyne signal is modulated with a sum frequency $\omega_1+\omega_2$ as τ is varied, in addition, the phase of the oscillation depends on the phase θ_B of the measured third-order susceptibility χ_B. If we adjust the time delay τ such that $\Delta\mathbf{k}\cdot\mathbf{r}-(\omega_1+\omega_2)|\tau|=2n\pi$, then

$$I_{ASPB}(\Delta_1,\tau)\propto I_C(\tau)+2L_8\eta|\chi_B|\cos\theta_B\propto I_C+2L_4\eta\chi_B'. \quad (28)$$

However, if $\Delta\mathbf{k}\cdot\mathbf{r}-(\omega_1+\omega_2)|\tau|=(2n-1/2)\pi$, we have

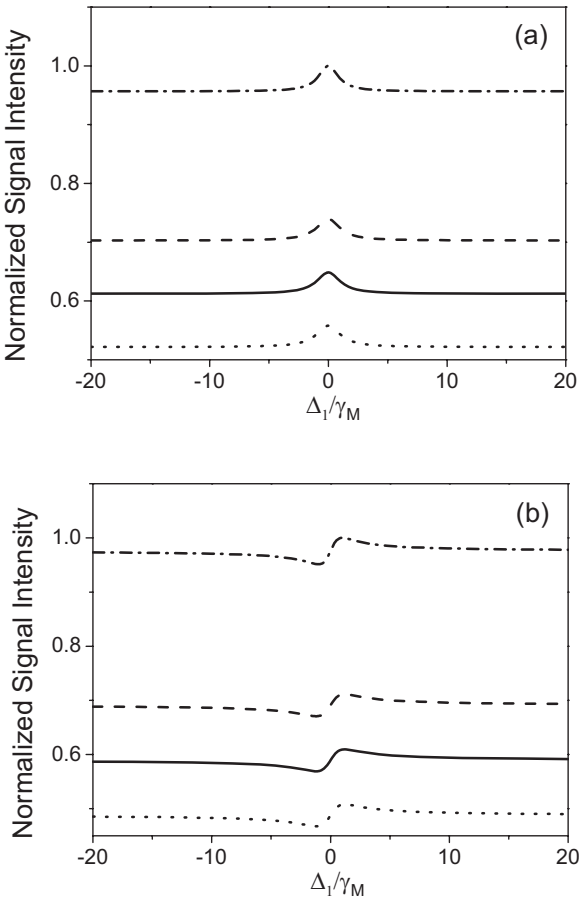

FIG. 13. The heterodyne detection spectra versus Δ_1/γ_M of the Rayleigh ASPB with (a) $\tau=(-2\pi+\Delta\mathbf{k}\cdot\mathbf{r})/(\omega_1+\omega_2)$ for the real part of χ_B, while with (b) $\tau=(-2\pi+\pi/2+\Delta\mathbf{k}\cdot\mathbf{r})/(\omega_1+\omega_2)$ for the imaginary part of χ_B. The other parameters are for $\chi_M/\chi_T=1$, $\gamma_M/\alpha_1=10$, $\gamma_T/\alpha_1=1\times10^{-5}$, $\alpha_2/\alpha_1=\alpha_3/\alpha_1=1$, $\eta=10$. Theoretical curves are shown in CFM (solid curve), PDM (dotted curve), GAM (dashed curve), and the model with cw laser beams (dotted-dashed curve).

$$I_{ASPB}(\Delta_1,\tau)\propto I_C(\tau)+2L_8\eta|\chi_B|\sin\theta_B\propto I_C(\tau)+2L_4\eta\chi_B''. \quad (29)$$

In other words, by changing the time delay τ between beams 1 and 2 we can obtain the real and the imaginary parts of the Rayleigh-enhanced susceptibility χ_B.

Figure 13 shows the heterodyne detection spectra versus Δ_1/γ_M of the Rayleigh ASPB. We can see that the spectra have the profile of the real and imaginary parts of the Rayleigh resonance with comparable backgrounds. It is clear that the curves represent the even function for the real part and the odd function for the imaginary part of χ_B, which is just the opposite to those of the Raman-enhanced susceptibility χ_A (Fig. 12). On the other hand, similarly, for heterodyne signal of Rayleigh ASPB the spectra of cw beams are the same as those of CFM, PDM, and GAM. However, the spectra of cw beams have the largest background while the spectra of PDM have the smallest background due to the absence of the amplitude fluctuation.

C. Coexisting of Raman and Rayleigh ASPB

The Raman- and Rayleigh-enhanced FWM can coexist in the same experiment system. In fact, they can be considered as the reference signal mutually. Thus, the coexisting of Raman- and Rayleigh ASPB signal is proportional to the average of the absolute square of P_A+P_B, so that the signal intensity $I(\Delta_1,\Delta_2,\tau)\propto\langle|P_A+P_B|^2\rangle$ contains $7\times7=49$ different terms where $I_{A,B}(\Delta_1,\Delta_2,\tau)=\langle P_AP_B^*\rangle+\langle P_AP_B^*\rangle$ include $u_i(t)$ second-order Markovian stochastic correlation functions. The cross-correlation terms are the same for three Markovian stochastic models but more complex than that of the pure Rayleigh and Raman ASPB. It consists of the third-order susceptibilities for the Rayleigh- and Raman-enhanced FWM, i.e., χ_A and χ_B.

In heterodyne detection, we can either assume $I_A(\Delta_2,\tau)\gg I_B(\Delta_1,\tau)$ $(\eta\gg1)$ to obtain $I\propto I_A(\Delta_2,\tau)+I_{A,B}(\Delta_1,\Delta_2,\tau)$ for studying the phase dispersion of the Rayleigh-enhanced third-order susceptibility χ_B [Figs. 14(a) and 14(b)] or assume $I_A(\Delta_2,\tau)\ll I_B(\Delta_1,\tau)$ $(\eta\ll1)$ to obtain $I\propto I_B(\Delta_1,\tau)+I_{A,B}(\Delta_1,\Delta_2,\tau)$ for studying the phase dispersion of the Raman-enhanced third-order susceptibility χ_A [Figs. 14(c) and 14(d), and Fig. 15].

Under the condition of $\gamma_R,\gamma_M\gg\alpha_1,\alpha_2,\alpha_3\gg\gamma_T$ and $\eta\gg1$ we have the coexisting Raman and Rayleigh ASPB signals for the three Markovian models, respectively, i.e.,

$$\begin{aligned}I_{ASPB}(\Delta_1,\Delta_2,\tau)\propto{}&\eta^2\exp(-2i\Delta\mathbf{k}\cdot\mathbf{r})\{[1+n_4\exp(-2\alpha_2|\tau|)]L_5\\&+L_6\}+\eta\exp[-(\alpha_1+\alpha_2)|\tau|]\\&\times\{\exp[i\Delta\mathbf{k}\cdot\mathbf{r}-i(\omega_1+\omega_2)|\tau|]\chi_A^*\chi_B\\&+\exp[-i\Delta\mathbf{k}\cdot\mathbf{r}+i(\omega_1+\omega_2)|\tau|]\chi_A\chi_B^*\}.\end{aligned}\tag{30}$$

Therefore, from Eq. (30) we have

$$\begin{aligned}I(\Delta_1,\Delta_2,\tau)\propto{}&I_A(\Delta_2,\tau)+2\eta\exp[-(\alpha_1+\alpha_2)|\tau|]|\chi_A||\chi_B|\\&\times\cos[\Delta\mathbf{k}\cdot\mathbf{r}-(\omega_1+\omega_2)|\tau|-\theta_A+\theta_B].\end{aligned}\tag{31}$$

Here $I_A(\Delta_2,\tau)=\eta^2\exp(-2i\Delta\mathbf{k}\cdot\mathbf{r})\{[1+n_4\exp(-2\alpha_2|\tau|)]\times L_5+L_6\}$. Equation (31) indicates that the reference Raman-enhanced FWM signal $I_A(\Delta_2,\tau)$, the factor $2\eta\exp[-(\alpha_1+\alpha_2)|\tau|]|\chi_A|$, and θ_A are independent of Δ_1. If we adjust the time delay τ such that $\Delta\mathbf{k}\cdot\mathbf{r}-(\omega_1+\omega_2)|\tau|-\theta_A=2n\pi$ [Figs. 14(a) and 14(c)], then

$$\begin{aligned}I(\Delta_1,\Delta_2,\tau)\propto{}&I_A(\Delta_2,\tau)+2\eta\exp[-(\alpha_1+\alpha_2)|\tau|]|\chi_A||\chi_B|\cos\theta_B\\={}&I_A(\Delta_2,\tau)+2\eta\exp[-(\alpha_1+\alpha_2)|\tau|]|\chi_A|\chi_B'.\end{aligned}\tag{32}$$

However, if $\Delta\mathbf{k}\cdot\mathbf{r}-(\omega_1+\omega_2)|\tau|-\theta_A=(2n-1/2)\pi$ [Figs. 14(b) and 14(d)], we have

$$\begin{aligned}I(\Delta_1,\Delta_2,\tau)\propto{}&I_A(\Delta_2,\tau)+2\eta\exp[-(\alpha_1+\alpha_2)|\tau|]|\chi_A||\chi_B|\sin\theta_B\\={}&I_A(\Delta_2,\tau)+2\eta\exp[-(\alpha_1+\alpha_2)|\tau|]|\chi_A|\chi_B''.\end{aligned}\tag{33}$$

In other words, by changing the time delay τ between beams 1 and 2 we can obtain the real and the imaginary parts of the Rayleigh-enhanced susceptibility χ_B. Figures 14(a) and 14(b) show the heterodyne detection spectra versus Δ_1/γ_M of the coexisting Raman and Rayleigh ASPB with large η. They are the same as Fig. 13 and only the reference backgrounds are different. Therefore, the spectra show the profile of the real and imaginary parts of the Rayleigh-enhanced susceptibility.

Similarly, under the condition of $\gamma_R,\gamma_M\gg\alpha_1,\alpha_2,\alpha_3\gg\gamma_T$ and $\eta\ll1$ we have the coexisting Raman and Rayleigh ASPB signals for the three Markovian models, respectively, i.e.,

$$\begin{aligned}I(\Delta_1,\Delta_2,\tau)\propto{}&\{[1+n_4\exp(-2\alpha_1|\tau|)]L_9+L_{10}\}\\&+\eta\exp[-(\alpha_1+\alpha_2)|\tau|]\\&\times\{\exp[i\Delta\mathbf{k}\cdot\mathbf{r}-i(\omega_1+\omega_2)|\tau|]\chi_A^*\chi_B\\&+\exp[-i\Delta\mathbf{k}\cdot\mathbf{r}+i(\omega_1+\omega_2)|\tau|]\chi_A\chi_B^*\}.\end{aligned}\tag{34}$$

From Eq. (34) we have

$$\begin{aligned}I(\Delta_1,\Delta_2,\tau)\propto{}&I_B(\Delta_1,\tau)+2\eta\exp[-(\alpha_1+\alpha_2)|\tau|]|\chi_B||\chi_A|\\&\times\cos[\Delta\mathbf{k}\cdot\mathbf{r}-(\omega_1+\omega_2)|\tau|-\theta_A+\theta_B].\end{aligned}\tag{35}$$

Here $I_B(\Delta_1,\tau)=[1+n_4\exp(-2\alpha_1|\tau|)]L_9+L_{10}$. The reference Rayleigh-enhanced FWM signal $I_B(\Delta_1,\tau)$, the factor $2\eta\exp[-(\alpha_1+\alpha_2)|\tau|]|\chi_B|$ and θ_B are independent of Δ_2. If we adjust the time delay τ such that $\Delta\mathbf{k}\cdot\mathbf{r}-(\omega_1+\omega_2)|\tau|+\theta_B=2n\pi$ [Fig. 14(c) Figs. 15(a)–15(c)], then

$$\begin{aligned}I(\Delta_1,\Delta_2,\tau)\propto{}&I_B(\Delta_1,\tau)+2\eta\exp[-(\alpha_1+\alpha_2)|\tau|]|\chi_B||\chi_A|\cos\theta_A\\={}&I_B(\Delta_1,\tau)+2\eta\exp[-(\alpha_1+\alpha_2)|\tau|]|\chi_B|\chi_A'.\end{aligned}\tag{36}$$

However, if $\Delta\mathbf{k}\cdot\mathbf{r}-(\omega_1+\omega_2)|\tau|+\theta_B=(2n+1/2)\pi$ [Fig. 14(d) and Figs. 15(d)–15(f)], we have

$$\begin{aligned}I(\Delta_1,\Delta_2,\tau)\propto{}&I_B(\Delta_1,\tau)+2\eta\exp[-(\alpha_1+\alpha_2)|\tau|]|\chi_B||\chi_A|\sin\theta_A\\={}&I_B(\Delta_1,\tau)+2\eta\exp[-(\alpha_1+\alpha_2)|\tau|]|\chi_B|\chi_A''.\end{aligned}\tag{37}$$

In other words, by changing the time delay τ between beams 1 and 2 we can obtain the real and the imaginary parts of the Raman-enhanced susceptibility χ_A. Figures 14(c) and 14(d) show the heterodyne detection spectra versus Δ_2/γ_R of the coexisting Raman and Rayleigh ASPB with small η. They are the same as Fig. 12 and only the reference backgrounds are different. Therefore, the spectra show the profile of the real and imaginary parts of the Raman-enhanced susceptibility. In addition, Fig. 15 shows the spectra versus Δ_1/γ_R and Δ_2/γ_R. The spectra mainly show the profile of Rayleigh-enhanced FWM signal versus Δ_1/γ_R. As $\Delta_1/\gamma_R=-5$ and τ satisfies the condition of $\Delta\mathbf{k}\cdot\mathbf{r}-(\omega_1+\omega_2)|\tau|+\theta_B=2n\pi$, the spectra versus Δ_2/γ_R show the real part of the Raman-enhanced susceptibility, while as $\Delta_1/\gamma_R=-5$ and τ satisfies the condition of $\Delta\mathbf{k}\cdot\mathbf{r}-(\omega_1+\omega_2)|\tau|+\theta_B=2n\pi+\pi/2$, the spectra versus Δ_2/γ_R show the imaginary part of the Raman-enhanced susceptibility.

VII. DISCUSSION AND CONCLUSION

Based on three stochastic models, the subtle Markovian, field-correlation effects have been investigated in Raman- and Rayleigh-enhanced FWM, homodyne- and heterodyne-detected ASPB. All of these can be understood in the time and frequency domains.

A. Field-correlation effects of three stochastic models

Ultrashort pulses of equivalent bandwidth are not immune to dispersive effects (even when balanced) because the trans-

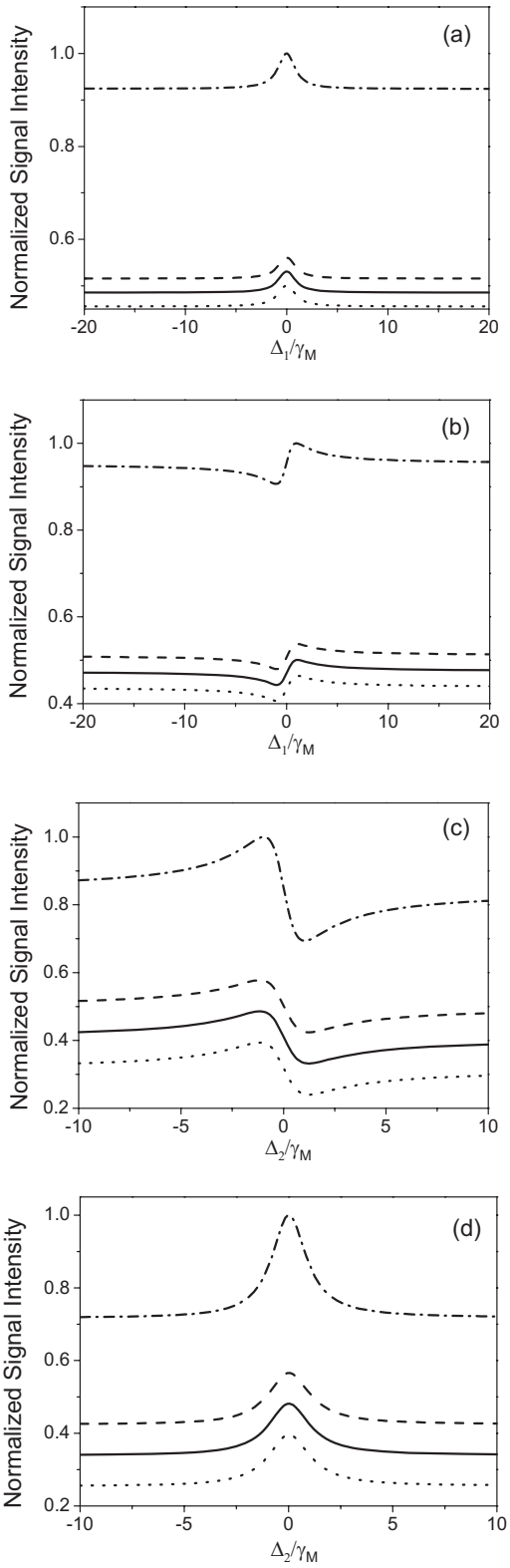

FIG. 14. The heterodyne detection spectra versus Δ_1/γ_M of the coexisting ASPB for $\chi_M/\chi_R=0.1$, $\gamma_M/\alpha_1=\gamma_R/\alpha_1=10$, $\chi_T/\chi_R=0.1$, $\gamma_T/\alpha_1=1\times10^{-5}$, $\alpha_2/\alpha_1=\alpha_3/\alpha_1=1$, (a) $\eta=10$, $\Delta_2/\gamma_R=10$, $\tau=(2n\pi+\Delta\mathbf{k}\cdot\mathbf{r})/(\omega_1+\omega_2)$ for the real part of χ_B, (b) $\eta=10$, $\Delta_2/\gamma_R=10$, $\tau=(2n\pi+\pi/2+\Delta\mathbf{k}\cdot\mathbf{r})/(\omega_1+\omega_2)$ for the imaginary part of χ_B, (c) $\eta=0.1$, $\Delta_1/\gamma_R=1$, $\tau=(2n\pi+\Delta\mathbf{k}\cdot\mathbf{r})/(\omega_1+\omega_2)$ for the real part of χ_A, (d) $\eta=0.1$, $\Delta_1/\gamma_R=1$, $\tau=(2n\pi+\Delta\mathbf{k}\cdot\mathbf{r})/(\omega_1+\omega_2)$ for the imaginary part of χ_A. Here $n=-10\,000$.

form limited light pulse is in fact temporally broadened (it is chirped) and this has drastic effects on its time resolution (the autocorrelation). In this sense the ASPB with double-frequency color-locking noisy light has an advantage [30–33]. Based on three stochastic models, the subtle Markovian field correlation effects have been investigated in the homodyne or heterodyne detected ASPB. The different roles of the amplitude fluctuations and the phase fluctuations can be understood in time- and frequency domains. The physical explanation for this is that the Gaussian-amplitude field undergoes stronger intensity fluctuations than a chaotic field. On the other hand, the intensity (amplitude) fluctuations of the Gaussian-amplitude field or the chaotic field are always much larger than the pure phase fluctuations of the phase-diffusion field. In fact, the difference of the spectra of the three Markovian stochastic models of the laser field can be controlled. Specifically, (i) at zero delay time it shows the drastic difference for three Markovian stochastic fields, while the PDM and GAM results are the same as those of the CFM in the limit of $|\tau|\to\infty$. It means that the fluctuation of both the amplitude and the phase of the field have no effect in the limit of $|\tau|\to\infty$. (ii) Under narrowband linewidth ($\alpha_i \ll \gamma_M, \gamma_T$), the difference value of the signal intensity at $\Delta_{1,2}=0$ among the three models is dramatic, however, it becomes smaller under broadband linewidth ($\alpha_i \gg \gamma_M, \gamma_T$). That is to say, stochastic correlation effects are sensitive to narrowband linewidth. (iii), As χ_T is small, the difference of the spectra of the three models is drastic, while the nonresonant thermal background is much larger than the resonant signal that the contribution from thermal grating dominates the FWM spectra and obscure the difference of the spectra of the three models.

B. Suppression of background

Both Raman- and Rayleigh-enhanced FWM are proposed for studying ultrafast processes. In contrast to the conventional time-domain technique, they are frequency-domain techniques, the time resolution is independent of the incident laser pulse width. Therefore, Raman- and Rayleigh-enhanced FWM can be employed for the measurement of ultrafast longitudinal relaxation time in the frequency-domain [7]. Based on the field-correlation effects, this technique can be applied even to an absorbing medium if a time-delayed method. There are two mechanisms involved. First, the nonlinear interaction of beams 1 and 2 with the same frequencies gives rise to the static gratings (molecular reorientation and thermal gratings). The FWM signal is the result of the diffraction of beam 3 by the grating. Second, beams 2 and 3 with different frequencies build up the moving gratings (Raman and Rayleigh modes). If the grating lifetime is larger than the time it needs to move over one spatial period, then destructive interference occurs during engraving and erases the grating.

Physically, for the coexisting Rayleigh- and Raman-enhanced FWM processes, the resonant signals originate from the order parameters $Q_{RM,RT,R}(\mathbf{r},t)$ while the nonresonant background come from both $Q_{M1,2}(\mathbf{r},t)$ and $Q_{T1,2}(\mathbf{r},t)$. The establishment of order parameters of the gratings in-

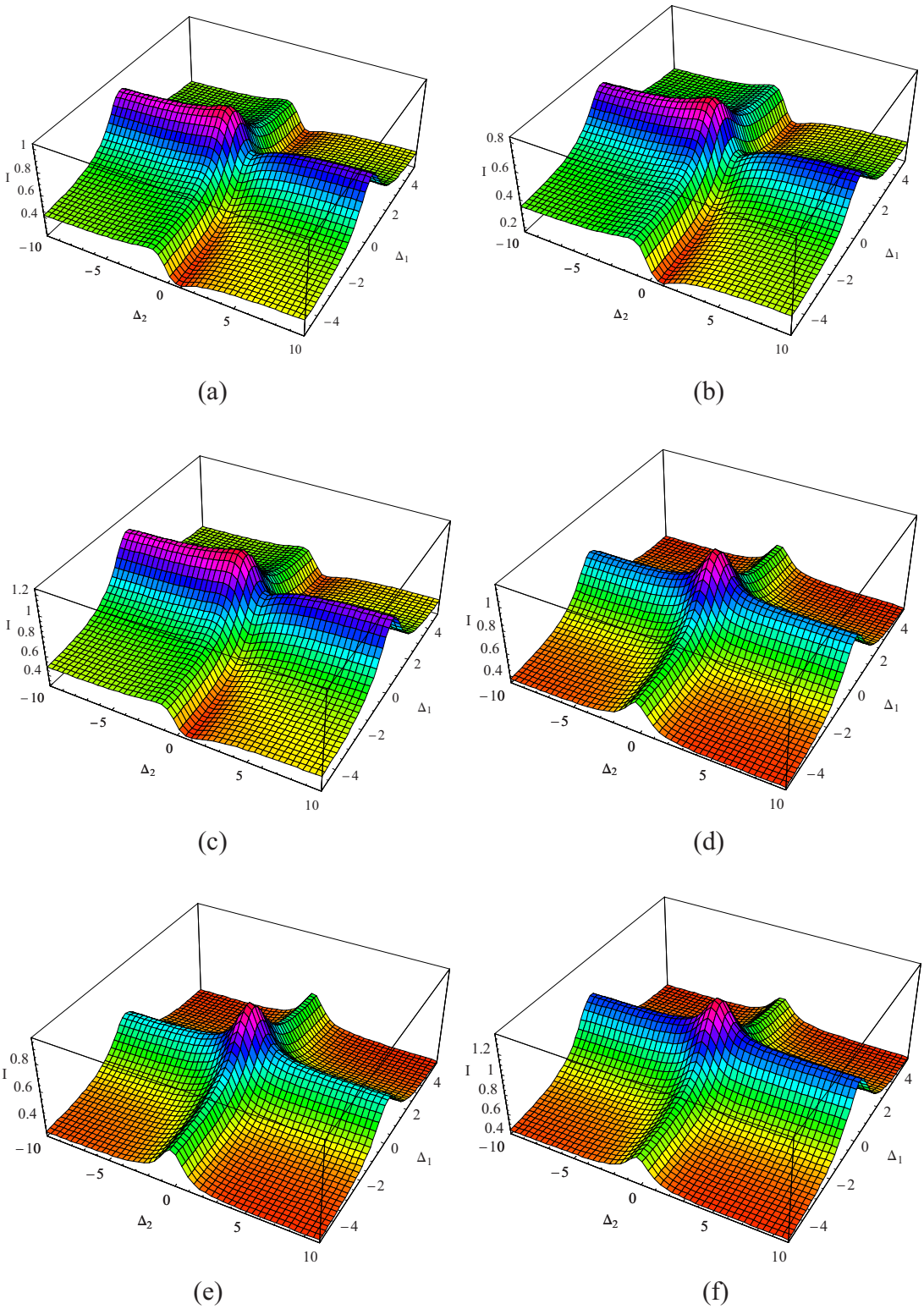

FIG. 15. (Color online) The heterodyne detection spectra versus Δ_1/γ_R and Δ_2/γ_R of the coexisting ASPB for $\eta=0.1$, $\chi_M/\chi_R=0.1$, $\gamma_M/\alpha_1=\gamma_R/\alpha_1=10$, $\chi_T/\chi_R=0.1$, $\gamma_T/\alpha_1=1\times10^{-5}$, $\alpha_2/\alpha_1=\alpha_3/\alpha_1=1$ with $\tau=(2n\pi-\Delta\mathbf{k}\cdot\mathbf{r}-\theta_B)/(\omega_1+\omega_2)$ and $(2n\pi+\pi/2-\Delta\mathbf{k}\cdot\mathbf{r}-\theta_B)/(\omega_1+\omega_2)$ for $\tau>0$ for the real and imaginary part of χ_A. Theoretical curves represent the (a) and (d) CFM, (b) and (e) PDM, (c) and (f) GAM. Here $n=-10\,000$.

volves integration effects. In the broadband case (i.e., $\alpha_{1,2,3} \gg \gamma_T, \gamma_M, \gamma_R$), the effect of integration is to wash out the gratings. At zero time delay no washout takes place in the establishment of $Q_{M1,2}(\mathbf{r},t)$ and $Q_{T1,2}(\mathbf{r},t)$ because the phase factor $\phi_{1,2}$ of $A_{1,2}(t-t')[A_{1,2}(t-t'-\tau)]^*$ is stationary. On the other hand, the phase factors ϕ_{3a} of $A_3(t-t')[A_1(t-t'-\tau)]^*$

and ϕ_{3b} of $A_3(t-t')[A_2(t-t')]^*$ are random variable which fluctuate with characteristic time scales $(\alpha_1+\alpha_3)^{-1}$ and $(\alpha_2+\alpha_3)^{-1}$, respectively. Because of the integration effect, the fast random fluctuation of $\phi_{3a,b}$ leads to the reduction of the amplitude of $Q_{RM,RT,R}(\mathbf{r},t)$. Therefore, the coexisting Rayleigh- and Raman-enhanced FWM spectra are dominated by a large nonresonant background when $\tau=0$. However, the coexisting Rayleigh- and Raman-enhanced FWM spectra are quite different in the limit of $\alpha|\tau| \gg 1$. Similar to $Q_{RM,RT,R}(\mathbf{r},t)$, $Q_{M1,2}(\mathbf{r},t)$ and $Q_{T1,2}(\mathbf{r},t)$ are now induced by mutually incoherent fields. If $\alpha_{1,2}=\alpha_3$, then the influences of the integration effect on them are equal [Fig. 2(b)]. Thus, the nonresonant backgrounds are suppressed effectively. We now consider the case when $\gamma_T, \gamma_M, \gamma_R \gg \alpha_{1,2,3}$. In this case, the gratings have quite short relaxation times, therefore, they can respond to the phase fluctuations of the fields almost immediately. More specifically, $A_{1,2}(t-t')[A_{1,2}(t-t'-\tau)]^*$, $A_3(t-t')[A_1(t-t'-\tau)]^*$, and $A_3(t-t')[A_2(t-t')]^*$ are slowly varying functions in comparison with $\exp(-\gamma_{M,T,R}t')$ which have a peak at $t'=0$, and therefore can be approximated as $A_{1,2}(t)[A_{1,2}(t)]^*$, $A_3(t)[A_1(t)]^*$, and $A_3(t)[A_2(t)]^*$, respectively. We have

$$P_{M1,2}(\mathbf{r},t) \propto \chi_M \gamma_M A_{1,2}(t)[A_{1,2}(t)]^* A_3(t) \int_0^\infty \exp(-\gamma_M t')dt',$$

$$P_{T1,2}(\mathbf{r},t) \propto \chi_T \gamma_T A_{1,2}(t)[A_{1,2}(t)]^* A_3(t) \int_0^\infty \exp(-\gamma_T t')dt',$$

$$P_{RM,RT}(\mathbf{r},t) \propto \chi_{M,T}\gamma_{M,T}A_1(t)[A_1(t)]^*A_3(t) \times \int_0^\infty \exp[-(\gamma_{M,T}-i\Delta_1)t']dt',$$

$$P_R(\mathbf{r},t) \propto \chi_R \gamma_R A_2(t)[A_2(t)]^* A_3(t) \int_0^\infty \exp[-(\gamma_R - i\Delta_2)t']dt'.$$

The above equation indicates that the Rayleigh- and Raman-enhanced FWM spectra are independent of τ.

C. Phase-sensitive detection

The Raman-enhanced FWM the Raman vibration is excited by the simultaneous presence of two incident beams whose frequency difference equals the Raman excitation frequency and the Raman-enhanced FWM signal is the result of this resonant excitation. In contrast, the Rayleigh-enhanced FWM process is a nonresonant process and a frequency-domain nonlinear laser spectroscopy with high frequency resolution determined by the laser linewidth. Moreover, the Rayleigh-enhanced FWM is a nonresonant process with no energy transfer between the lights and the medium when the frequency difference between two incident beams equals zero. The resonant structure in the Rayleigh-enhanced FWM spectrum is the result of induced moving grating. This difference is also reflected in their line shapes. Specifically, unlike the Raman-enhanced FWM spectrum, which is asymmetric due to the interference between the resonant signal and the nonresonant background, the line shape of the Rayleigh-enhanced FWM is always symmetric.

In this paper we employ the ASPB to obtain the real and the imaginary parts of the competition Raman and Rayleigh resonance (Fig. 14) based on the polarization interference between coexistence of Raman- and Rayleigh-enhanced FWM processes. Specifically, since Raman- and Rayleigh-enhanced FWM signals propagate along the same optical path, in the heterodyne detection of ASPB, we purposely introduce them as the reference signals of each other. Our method is based on polarization interference between two competition Raman- and Rayleigh-enhanced FWM processes. The detuning Δ_1 and Δ_2 control the intensity and phase angle of Rayleigh- and Raman-enhanced susceptibilities χ_B and χ_A, respectively [36–38]. We need scanning one detuning to show the phase dispersion of χ_B or χ_A with proper time delay, while the other one only to change the reference background. If Δ_1 or Δ_2 change large enough, the value of θ_B or θ_A will equal zero and the coexisting Raman and Rayleigh ASPB will convert into the pure Raman or Rayleigh ASPB.

D. Proposed experiment

One possible experimental candidate for the proposed system is the sample of benzene in which oxazine dye is dissolved. The strong vibration mode of benzene is at $\Omega_R = 992\ \mathrm{cm}^{-1}$. The Raman mode can be activated in benzene. In addition, the static molecular-reorientation grating and the corresponding Rayleigh mode also exist in such material. On the other hand, the oxazine dye introduces the static thermal grating and the corresponding Rayleigh mode. Therefore, we can study the competition of Raman- and Rayleigh-enhanced FWM and ASPB mediated by thermal effects.

Such an experiment can be done by using three nanosecond dye lasers (color locking) or femtosecond ultrashort lasers (phase locking) $D1$, $D2$, and $D3$. $D1$ and $D2$ are used to generate frequencies at ω_1 and ω_2, respectively. A beam splitter is used to combine the ω_1 and ω_2 components for the pump beams. Beam 1 and beam 2 intersected in the sample with a small angle between them. The relative time delay between beams 1 and 2 can be varied by an optical delay line controlled by a stepping motor. Beam 3, used as the probe beam and originating from $D3$ with frequency ω_3, propagating along the direction opposite that of beam 1.

More specifically, (i) for the coexisting Raman and Rayleigh ASPB, $D1$, $D2$, and $D3$ have the wavelengths $\lambda_1 = 561$ nm, $\lambda_2 = 532$ nm, and $\lambda_3 = 561$ nm, respectively. Thus, the Raman mode is activated by the interaction of beam 3 and ω_2 component of beam 2. As a result, Raman-enhanced FWM is generated. On the other hand, the Rayleigh-enhanced FWM is generated due to the interaction of beam 3 and ω_1 component of beam 2. Both ω_1 and ω_2 frequencies can be varied. (ii) For the Raman ASPB, $D1$, $D2$, and $D3$ have the wavelength $\lambda_1 = 565$ nm, $\lambda_2 = 532$ nm, and $\lambda_3 = 561$ nm, respectively. Thus only the Raman mode is activated by the interaction of beam 3 and ω_2 component of beam 2. As a result, Raman-enhanced FWM is generated accompanying NDFWM resulting from diffraction by the

static molecular-reorientation and thermal gratings due to the interaction of beam 3 and ω_1 component of beam 2. The ω_2 frequency can be varied. (iii) For the Rayleigh ASPB, $D1$, $D2$, and $D3$ have the wavelength $\lambda_1=561$ nm, $\lambda_2=565$ nm, and $\lambda_3=561$ nm, respectively. Thus only the Rayleigh-enhanced FWM is generated due to the interaction of beam 3 and ω_1 component of beam 2, while NDFWM due to the interaction of beam 3 and component of beam 2 is generated and used as a reference signal. The ω_1 frequency can be varied.

In addition, there exist two types of polarization configuration: (i) Beam 1 was polarized along the direction and beams 2 and 3 were polarized along the y direction. The FWM signal, which was polarized along the x direction, propagated along a direction almost opposite that of beam 2 (Fig. 1). In such case no thermal grating is generated because the two pump beams 1 and 2 are perpendicular to each other. (ii) Beams 1, 2, and 3 were polarized along the x direction. The FWM signal was polarized along the x direction. Here, both thermal grating and molecular-reorientation grating are induced. The nonresonant background can be suppressed dramatically by increasing the relative time-delay (successfully controlling field correlation). There still exists the residual nonresonant background due to the molecular-reorientation grating. In this work [case (ii)], we consider the influence of the thermal grating to the coexisting Raman- and Rayleigh-enhanced FWM and the time-delayed method to suppress the thermal nonresonant background.

E. Conclusion

In summary, based on color-locking noisy field correlation, the subtle Markovian field correlation effects in three stochastic models have been investigated in studying the Raman- and Rayleigh-enhanced FWM. One interesting feature in field-correlation effects is that Rayleigh-enhanced FWM exhibits spectral symmetry, while Raman-enhanced FWM exhibits spectral asymmetry due to the interference between the resonant mode and the nonresonant background. We also note that Raman-enhanced FWM exhibits temporal asymmetry with hybrid radiation-matter detuning terahertz damping oscillation. In addition, a time-delayed method to suppress the background is mentioned in a Kerr medium and an absorbing medium. On the other hand, based on the three stochastic models, homodyne (quadratic) and heterodyne (linear) detection of the Raman ASPB, the Rayleigh ASPB, and the coexisting Raman and Rayleigh ASPB have also been investigated, respectively.

ACKNOWLEDGMENTS

We acknowledge support from the National Natural Science Foundation of China (Grant No. 60678005), the Author of National Excellent Foundation (Grant No. 200339), the Ying-Tong Education Foundation (Grant No. 101061), and the Specialized Research Foundation (Grant No. 20050398017).

[1] N. Morita and T. Yajima, Phys. Rev. A **30**, 2525 (1984).
[2] T. F. Schulz, P. P. Aung, L. R. Weisel, K. M. Cosert, M. W. Gealy, and D. J. Ulness, J. Opt. Soc. Am. B **22**, 1052 (2005).
[3] D. J. Ulness, J. Phys. Chem. A **107**, 8111 (2003).
[4] J. C. Kirkwood, D. J. Ulness, and A. C. Albrecht, J. Phys. Chem. A **104**, 4167 (2000).
[5] E. C. Booth, B. G. Berger, Z. C. Johnson, T. M. Ta, L. R. Weisel, and D. J. Ulness, J. Opt. Soc. Am. B **23**, 885 (2006).
[6] D. C. DeMott, D. J. Ulness, and A. C. Albrecht, Phys. Rev. A **55**, 761 (1997).
[7] D. J. Ulness and A. C. Albrecht, J. Raman Spectrosc. **28**, 571 (1997).
[8] M. J. Stimson, D. J. Ulness, and A. C. Albrecht, J. Raman Spectrosc. **28**, 579 (1997).
[9] M. J. Stimson, D. J. Ulness, J. C. Kirkwood, and G. S. Boutis, J. Opt. Soc. Am. B **15**, 505 (1998).
[10] Y. P. Zhang, A. W. Brown, and M. Xiao, Phys. Rev. Lett. **99**, 123603 (2007).
[11] Y. Wu, J. Saldana, and Y. F. Zhu, Phys. Rev. A **67**, 013811 (2003).
[12] R. E. Ryan and T. H. Bergeman, Phys. Rev. A **43**, 6142 (1991).
[13] C. Chen, D. S. Elliott, and M. W. Hamilton, Phys. Rev. Lett. **68**, 3531 (1992).
[14] R. Walser, H. Ritsch, P. Zoller, and J. Cooper, Phys. Rev. A **45**, 468 (1992).
[15] R. E. Ryan, L. A. Westling, R. Blumel, and H. J. Metcalf, Phys. Rev. A **52**, 3157 (1995).
[16] Cheng Xie, G. Klimeck, and D. S. Elliott, Phys. Rev. A **41**, 6376 (1990).
[17] A. T. Georges, Phys. Rev. A **21**, 2034 (1980).
[18] R. Bratfalean and P. Ewart, Phys. Rev. A **56**, 2267 (1997).
[19] Y. R. Shen, *The Principles of Nonlinear Optics* (Wiley, New York, 1984) Chaps. 10, 15, and 16.
[20] G. Martin and R. W. Hellwarth, Appl. Phys. Lett. **34**, 371 (1979).
[21] P. M. Fu, Z. H. Yu, X. Mi, Q. Jiang, and Z. G. Zhang, Phys. Rev. A **46**, 1530 (1992).
[22] P. M. Fu, Q. Jiang, X. Mi, and Z. H. Yu, Phys. Rev. Lett. **88**, 113902 (2002).
[23] Y. P. Zhang, X. Hou, K. Q. Lu, and H. C. Wu, Opt. Commun. **184**, 265 (2000).
[24] Y. P. Zhang, C. L. Gan, K. Q. Lu, C. S. Li, and X. Hou, Opt. Commun. **205**, 163 (2002).
[25] Y. P. Zhang, C. L. Gan, J. P. Song, X. J. Yu, R. Q. Ma, H. Ge, C. S. Li, and K. Q. Lu, J. Opt. Soc. Am. B **22**, 694 (2005).
[26] Y. P. Zhang, C. L. Gan, L. Li, R. Q. Ma, J. P. Song, T. Jiang, X. J. Yu, C. S. Li, H. Ge, and K. Q. Lu, Phys. Rev. A **72**, 013812 (2005).
[27] D. DeBeer, E. Usadi, and S. R. Hartmann, Phys. Rev. Lett. **60**, 1262 (1988).
[28] V. L. Bogdanov, A. B. Evdokimov, G. V. Lukomskil, and B. D. Falnberg, JETP Lett. **49**, 157 (1989).
[29] H. Ma, A. S. L. Gomes, and Cid B. de Araujo, Opt. Lett. **17**,

1052 (1992).
[30] Y. P. Zhang, C. L. Gan, J. P. Song, X. J. Yu, R. Q. Ma, H. Ge, C. S. Li, and K. Q. Lu, Phys. Rev. A **71**, 023802 (2005).
[31] Y. P. Zhang, L. Q. Sun, T. T. Tang, and P. M. Fu, Phys. Rev. A **61**, 053819 (2000).
[32] Y. P. Zhang, T. T. Tang, L. Q. Sun, and P. M. Fu, Phys. Rev. A **61**, 023809 (2000).
[33] Y. P. Zhang, C. B. de Araujo, and E. E. Eyler, Phys. Rev. A **63**, 043802 (2001).
[34] J. W. Goodman, *Statistical Optics* (Wiley, New York, 1985), Chap 2.
[35] B. Picinbono and E. Boileau, J. Opt. Soc. Am. **58**, 784 (1968).
[36] M. Xiao, Y. Q. Li, S. Jin, and J. Gea-Banacloche, Phys. Rev. Lett. **74**, 666 (1995).
[37] C. L. Gan, M. Xiao, D. Battaglia, N. Pradham, and X. G. Peng, Appl. Phys. Lett. **91**, 201103 (2007).
[38] C. L. Gan, Y. P. Zhang, D. Battaglia, X. G. Peng, and M. Xiao,Appl. Phys. Lett. **92**, 241111 (2008).